Geoscientific
Model Development
Discussions

A nonhydrostatic oceanic regional model ORCTM v1 for internal solitary wave simulation

Hao Huang[1], Pengyang Song[1,2], Shi Qiu[1], Jiaqi Guo[1], Xueen Chen[1]

[1]College of Oceanic and Atmospheric Sciences, Ocean University of China, Qingdao, 266100, China

[2]Alfred Wegener Institute for Polar and Marine Research, Bremerhaven, Germany

Correspondence to: Xueen Chen (xchen@ouc.edu.cn)

Abstract.

An Oceanic Regional Circulation and Tide Model (ORCTM version 1) including the nonhydrostatic dynamics module which can numerically reproduce the Internal Solitary Waves (ISWs) dynamics, is presented in this paper. The model open boundary conditions are also supportive of regional baroclinic tidal wave simulations.

The incompressible Boussinesq equations in z-coordinates consider the three-dimensional and fully nonlinear forms. The pressure field is also decomposed into the surface, hydrostatic and nonhydrostatic components on the orthogonal curvilinear Arakawa-C grid. The nonhydrostatic pressure determined by the intermediate velocity divergence field is obtained via solving a three-dimensional Poisson equation based on a pressure correction method. Model validation experiments for ISWs simulations with the topographic change in the two-layer and continuously stratified ocean demonstrate that the ORCTM has a considerable capacity for reproducing the life cycle of Nonlinear Internal Waves evolution and tide-topography interactions.

1. Introduction

Internal Waves (also called Internal Gravity Waves) activities have been observed frequently across the stratified ocean and play a significant role in the multiscale energy cascade (Mtfller, 1976). Observations reveal that the Internal Waves, especially the high-frequency Internal Solitary Waves, could contain significant potential energy with strong vertical shear, mixing, and wave breaking, leading to a dramatic change of the currents and density structures (Ramp et al., 2004; Vlasenko et al., 2010; Huang et al., 2016), violent overturning bringing sediment and nutrient from the seafloor to the surface (Wang et al., 2007), even irretrievable damages to some underwater vehicles (Duda et al., 2006) and deep-water

28   drilling (Osborne et al., 1978). Basically, astronomical tides passing the abrupt topography can cause the

29   generation of the baroclinic tides (also called internal tides) with multi-modal structures then capable of

30   propagation, disintegration, and dissipation in the ocean (Vlasenko et al., 2005; 2010). The low-mode of

31   baroclinic tides can travel thousands of kilometers with the long horizontal wavelengths about ten of

32   kilometers (Baines, 1982). Furthermore, the inclusion of nonlinear and nonhydrostatic effects permits

33   the evolution of the Nonlinear Internal Waves (hereafter NIWs) even the Internal Solitary Waves

34   (hereafter ISWs) derived from the steepening of low-mode internal tides as the consequence of the ever-

35   changing terrain and background stratification (Gerkema and Zimmerman, 1995; legg and Adroft, 2003).

36   Numerical Ocean models are one of the most effective tools to study Internal Waves compared to

37   theoretical methods, in-situ observations, and laboratory investigations. Specifically, the ocean models

38   with the hydrostatic balance approximation have been used to explore the circulation and tide processes

39   across the stratified ocean thanks to their excellent performance with fairly high accuracy (Marshall et

40   al., 1997b; Chen et al., 2003; Shchepetkin and McWilliams, 2005; Ko et al., 2008). However, the high-

41   frequency nonlinear ISWs and the steepening of the internal tides cannot be depicted by the hydrostatic

42   models, because the strong vertical current with its order of magnitude equals the horizontal one via the

43   scale analysis method (Marshall et al., 1997a), when the three-dimensional Navier-Stokers equations

44   should be considered thoroughly. In other words, hydrostatic approximation due to omitting other terms

45   in the vertical momentum equation results in the inapplicability of the nonhydrostatic dynamics (Lai et

46   al., 2010). Thus, it is indispensable for simulating the nonlinear and large amplitude ISWs to develop a

47   nonhydrostatic ocean model and consider nonhydrostatic dynamics.

48   A robust ocean model considering the nonhydrostatic dynamics should satisfy two requirements

49   synchronously at least: 1) The high enough accuracy of meso-to-big scales simulation must be under

50   guarantee, such as the large-scale wind-induced circulation and mesoscale eddies reconstructed and

51   mainly influenced by the hydrostatic balance; 2) Meanwhile, it is the concerned small-meso scales with

52   the higher spatial and temporal resolution that are resolved finely under the nonhydrostatic balance, for

53   example, there is the simulation being able to describe the cradle-to-grave process for the tide-topography

54   interactions, the dispersive effects and nonlinear steepening of the baroclinic tides, and the breaking and

55   dissipation of strong nonlinear ISWs. The nonhydrostatic simulation can apply to the small-to-big scales

56   across the stratified ocean simultaneously, which can be assumed as one of the directions for research

57   and development of the nonhydrostatic ocean model. In reality, there have been some nonhydrostatic

58 ocean models or ones considering nonhydrostatic dynamics coming out in the past years, such as

59 MITgcm (Marshall et al., 1997a;1997b;1998), SUNTANS (Fringer et al., 2006), and ROMS (Kanarska

60 et al., 2007). All above have been used to realize a series of two or three-dimensional nonhydrostatic

61 numerical studies, including the instability of small-scale flows in the laboratory experiment (Lai et al.,

62 2010; Li et al., 2022), Internal Solitary Waves in the continental shelves (Vlasenko et al., 2010, Zeng et

63 al., 2019) and the hydraulic Lee wave around the seamount (Kanarska et al., 2007; Liu et al., 2016), etc.

64 Nevertheless, there is still no widespread use for the nonhydrostatic ocean model due to costly

65 computational resources. The corresponding nonhydrostatic solution to an extensive sparse linear

66 equation system is too difficult to solve directly for the 3-D oceanic environment, which usually demands

67 of large amounts of iteration times, fast convergent speed, and PC storage occupation. In addition, the

68 different kinds of sub-grid parameterization schemes have a profound impact on the model results with

69 a necessity for appropriate one to be assessed, and most of these model codes are seldom shared or of

70 open source. Suppose we develop a nonhydrostatic ocean model based on an original hydrostatic

71 framework model. In that case, the nonhydrostatic module will include the vertical momentum equation

72 with some terms related to the vertical velocity simultaneously complemented in the horizontal

73 momentum equation. Besides, based on the idea of the fractional step method (Press et al., 1988;

74 Armfield and Street, 2002), the total pressure is to be decomposed into hydrostatics and nonhydrostatic

75 components (Marshall et al., 1997a; Lai et al., 2010). The former corresponds to the result of hydrostatic

76 balance, and the divergence for intermediate velocity limits the latter to correct the local velocity fields

77 called the "pressure correction" method (Stansby and Zhou, 1998; Fringer et al., 2006; Kanarska et al.,

78 2007; Lai et al., 2010). With these methods, the nonhydrostatic dynamics simulation can be fulfilled

79 economically comparatively in harmony with the original physical framework as an extension of the

80 hydrostatic ocean model.

81   In this context, we have implemented the nonhydrostatic dynamic algorithm into an Oceanic

82 Regional Circulation and Tide Model (hereafter ORCTM) and demonstrated its ability and performance

83 of reproducing the life cycle of ISWs and NIWs in different hydrodynamic environments. The rest of the

84 paper is organized as follows. In Section 2, the basic framework of the ORCTM including control

85 equations, open boundary conditions, and nonhydrostatic algorithms is described. In Section 3, a series

86 of numerical validation experiments results are presented, aiming at the simulation of the overall

87 processes of the ISWs. In the last section, we come to conclusions and prospect the directions.

88   **2. Model development**

89   Derived from the basic framework of the Max-Planck-Institute ocean model featuring the global

90   hydrostatic modelling with the staggered Arakawa-C grid and the cartesian coordinates system

91   supporting the orthogonal curvilinear form (Marsland et al., 2003; Chen et al., 2005), in this paper, the

92   latest Max-Planck-Institute ocean model has been upgraded to realize the circulation and tide simulation

93   with the open boundary conditions for regional ocean modelling, and the z-level grid applied has the

94   partial filled cell capability to adjust the distance of the vertical grid on seabed for fitting into the realistic

95   terrain, which will be referred to hereafter as ORCTM. It is under the laws of the Boussinesq, rotating

96   and fully nonlinear Navier–Stokes fluid that the ORCTM can be used to study both the hydrostatic and

97   nonhydrostatic ocean dynamics, which namely can reproduce the nonhydrostatic dynamic processes such

98   as upwelling and downwelling, NIWs, and ISWs, etc.

99   **2.1. Control Equations**

100   The primitive three-dimensional control equations include the momentum, continuity, free surface,

101   potential temperature, salinity, and density equations given as follows.

$$\frac{\partial u}{\partial t} + u\frac{\partial u}{\partial x} + v\frac{\partial u}{\partial y} + w\frac{\partial u}{\partial z} - fv + \tilde{f}w = -\frac{1}{\rho_c}\frac{\partial P}{\partial x} - g\frac{\partial \varsigma}{\partial x} + F_{Vx} + F_{Hx} + \mathcal{F}_x \tag{1}$$

$$\frac{\partial v}{\partial t} + u\frac{\partial v}{\partial x} + v\frac{\partial v}{\partial y} + w\frac{\partial v}{\partial z} + fu = -\frac{1}{\rho_c}\frac{\partial P}{\partial y} - g\frac{\partial \varsigma}{\partial y} + F_{Vy} + F_{Hy} + \mathcal{F}_y \tag{2}$$

$$\frac{\partial w}{\partial t} + u\frac{\partial w}{\partial x} + v\frac{\partial w}{\partial y} + w\frac{\partial w}{\partial z} - \tilde{f}u = -\frac{1}{\rho_c}\frac{\partial P}{\partial z} - g + F_{Vz} + F_{Hz} + \mathcal{F}_z \tag{3}$$

$$\frac{\partial u}{\partial x} + \frac{\partial v}{\partial y} + \frac{\partial w}{\partial z} = 0 \tag{4}$$

$$\frac{\partial \varsigma}{\partial t} = -\nabla_h \cdot \int_{-H}^{\varsigma} \boldsymbol{u}_H dz \tag{5}$$

$$\frac{\partial \theta}{\partial t} + u\frac{\partial \theta}{\partial x} + v\frac{\partial \theta}{\partial y} + w\frac{\partial \theta}{\partial z} = F_{V\theta} + F_{H\theta} + Q_\theta \tag{6}$$

$$\frac{\partial S}{\partial t} + u\frac{\partial S}{\partial x} + v\frac{\partial S}{\partial y} + w\frac{\partial S}{\partial z} = F_{VS} + F_{HS} + Q_s \tag{7}$$

$$\rho = \rho(\theta, S, P) \tag{8}$$

102   In the cartesian coordinates system, t is the time; $\partial/\partial t$ is the time partial derivative; x, y and z

103   axes direct eastward, northward, and upward respectively; The horizontal velocity vector is $\boldsymbol{u_h} = (u, v)$;

104   w is the vertical velocity; ς is the change of the free surface elevation; P, θ and S are pressure,

105   potential temperature and salinity; ρ_c is the reference density of sea water under the Boussinesq

106   approximation; The first and second Coriolis parameters are $f = 2\Omega \sin\varphi$ and $\tilde{f} = 2\Omega \cos\varphi$, where Ω

107   is the rotational angular speed and φ is the geographic latitude. ∇_H is the horizontal divergence

108   operator; Q_θ and Q_s are source or sink terms about potential temperature and salinity. The equation of

109   seawater state is the polynomial form for the density ρ advocated by the Joint Panel on Oceanographic

110   Tables and Standards (Fofanoff and Millard, 1983).

111   The additional forcing term vector $\boldsymbol{\mathcal{F}} = (\mathcal{F}_x, \mathcal{F}_y, \mathcal{F}_y)$ can consider tidal potential forcing, river

112   runoff, and open boundary outflow and inflow. The horizontal eddy viscosity vector is $\boldsymbol{F}_H =$

113   (F_{Hx}, F_{Hy}, F_{Hy}) described with the scale-dependent biharmonic formulation (Wolff et al., 1997;

114   Marsland et al., 2003), and the horizontal diffusivity terms of temperature and salinity are $F_{H\theta}$ and

115   F_{HS} supporting the harmonic forms. Besides, the vertical eddy viscosity vector is $\boldsymbol{F}_V = (F_{Vx}, F_{Vy}, F_{Vy})$

116   and eddy diffusivity terms are $F_{V\theta}$ and F_{VS}. Here, the vertical eddy turbulent frictions which both are

117   specified to depend on the Richardson number Ri via the modified PP81 parameterization scheme

118   (Pacanowski and Philander, 1981). The viscous terms all above are expressed as

$$\boldsymbol{F}_H = -\nabla_h \cdot (B_H \nabla_h \Delta \boldsymbol{u}), \quad \boldsymbol{F}_V = \frac{\partial}{\partial z}\left(A_V \frac{\partial \boldsymbol{u}}{\partial z}\right) \tag{9}$$

$$F_{\gamma H} = D_H \Delta \gamma, \quad F_{\gamma V} = \frac{\partial}{\partial z}\left(D_V \frac{\partial \gamma}{\partial z}\right), \quad \gamma = \theta, S \tag{10}$$

$$A_V^{n+1} = (1-\lambda)A_V^n + \lambda(A_{V0}(1+\alpha \cdot Ri)^{-2} + A_w + A_b) \tag{11}$$

$$D_V^{n+1} = (1-\lambda)D_V^n + \lambda(D_{V0}(1+\alpha \cdot Ri)^{-3} + D_w + D_b) \tag{12}$$

$$Ri = \frac{N(z)^2}{(\partial u/\partial z)^2 + (\partial v/\partial z)^2} \tag{13}$$

119   where $\Delta = \nabla_h \cdot \nabla_h$ is the horizontal Laplace operator; B_H and D_H are parameterized with the horizontal

120   grid resolution; $N(z)$ is the buoyancy frequency. A_V^{n+1} and D_V^{n+1} are updated on formulas (11) and (12)

121   with the time relaxation coefficient λ at every timestep. Apart from the background viscous coefficients

122   A_b and D_b due to internal waves breaking, the modified PP81 scheme also considers the wind-induced

123   turbulent coefficients A_w and D_w associated with the local mixed layer depth and 10m wind speed

124   (Marsland et al., 2003). Here, the constant number α is set to be 5. And the adjustable parameters A_{V0}

125   and D_{V0} can be determined by estimating energy flux at every grid point. As for the boundary condition,

126   the slip conditions are specified at surface and bottom boundaries where the wind stress $\boldsymbol{\tau_w}$ is based on

127   the input, and the bottom drags $\boldsymbol{\tau_b}$ are described by linear and quadratic functions (Arbic and Scott, 2008).

Geoscientific
Model Development
Discussions

Open Access

2.2. Settings of Open Boundary Condition

128

129   It is fundamental for the regional model to be configured by an open boundary condition that avoids

130   reflection waves effectively so that the outward waves can freely flow through the boundaries.

131   Meanwhile, the external inputs such as the tidal waves can stably force the model domain through the

132   boundaries, satisfying the needs for consistency in hydrodynamics and computational mathematics. Here,

133   we use the relaxation boundary conditions with sponge layers consulting Zhang et al. (2011) that enable

134   to dampen the reflection waves in the model domain and refrain from the sharp gradients of water

135   properties caused by the prescribed boundary values on the boundaries. Specifically, we add a relaxation

136   term M formularized with the exponential function to the right-hand side of momentum equations (1)

137   to (3), temperature equation (6), and salinity equation (7) expressed as

$$M(x,y,z,t) = -\left(\frac{m(x,y,z,t) - m_b(x,y,z,t)}{\tau}\right) \cdot e^{-\frac{4 \cdot r(x,y)}{L_{sp}}} \tag{14}$$

138   In this formula (14), m_b is the boundary values of requisite model variables through the boundaries

139   including velocity, potential temperature, and salinity; m is the corresponding relaxation result in the

140   interiors; r is the distance from the boundary. Moreover, τ and L_{sp} are artificially prescribed adjustment

141   parameters referring to the time-scale coefficient and the thickness of the sponge layers. The model target

142   variables over the sponge layer will relax exponentially to the boundary values through the relaxation

143   term, where relaxation is modulated by τ and L_{sp} in the exponential shape. To restrain the reflection of

144   outflow current, τ and L_{sp} need to be determined in advance via estimating the energy flux of internal

145   signals through the boundaries. This open boundary relaxation condition is suitable for the numerical

146   study of the large ISWs so that the strong, nonlinear, and nonhydrostatic wave and current signals will

147   dampen gradually.

2.3. Implement of Nonhydrostatic Algorithms

148

149   According to the momentum equations (1) to (3), the total pressure P consists of sea surface

150   pressure p_s, hydrostatic pressure p_h, and nonhydrostatic pressure p_{nh} given as follows.

$$P = p_s(x,y) + p_h(x,y,z) + p_{nh}(x,y,z) \tag{15}$$

$$-\frac{1}{\rho_c}\frac{\partial p_h}{\partial z} - g = 0 \tag{16}$$

151   Hydrostatic pressure p_h can be calculated from the hydrostatic balance Eq. (16). It is negligible

152   for sea surface pressure term p_s to impact on the water column if the external atmospheric forcing is

153   excluded. Furthermore, based on the idea of the fractional step method (Press et al., 1988; Kanarska et

154   al., 2007), the intermediate velocity field $\tilde{\boldsymbol{u}}$ will be updated via the nonhydrostatic pressure p_{nh}^n

155   gradients, which is defined and can be obtained via the Eqs. (17) to (19) discretized as follows.

$$\frac{\tilde{u} - u^n}{\Delta t} = -G_x - \frac{1}{\rho_c}\frac{\partial p_{nh}^n}{\partial x} \tag{17}$$

$$\frac{\tilde{v} - v^n}{\Delta t} = -G_y - \frac{1}{\rho_c}\frac{\partial p_{nh}^n}{\partial y} \tag{18}$$

$$\frac{\tilde{w} - w^n}{\Delta t} = -G_z - \frac{1}{\rho_c}\frac{\partial p_{nh}^n}{\partial z} \tag{19}$$

156   Where the superscript *n* means the current timestep and the vector $\boldsymbol{G} = (G_x, G_y, G_y)$ represents the

157   advection terms, Coriolis terms, eddy viscosity terms, and hydrostatic pressure gradients terms.

158   Subsequently, the discretized partial equations (20) to (22) are established with the relationship between

159   the nonhydrostatic pressure perturbation p_{nh}' gradients and the next timestep *n*+1 velocity field. Then

160   nonhydrostatic pressure at the next timestep *n*+1 is defined as (23) in the light of the pressure correction

161   method. To obtain nonhydrostatic pressure perturbation the continuity equation (4) needs to be

162   substituted into Eqs. (20) to (22) to eliminate the following timestep *n*+1 velocity field with the three-

163   dimensional Poisson equation (24), which demonstrates that the nonhydrostatic pressure depends on the

164   vanishes of the divergence-free velocity fields.

$$\frac{u^{n+1} - \tilde{u}}{\Delta t} = -\frac{1}{\rho_c}\frac{\partial p_{nh}'}{\partial x} \tag{20}$$

$$\frac{v^{n+1} - \tilde{v}}{\Delta t} = -\frac{1}{\rho_c}\frac{\partial p_{nh}'}{\partial y} \tag{21}$$

$$\frac{w^{n+1} - \tilde{w}}{\Delta t} = -\frac{1}{\rho_c}\frac{\partial p_{nh}'}{\partial z} \tag{22}$$

$$p_{nh}^{n+1} = p_{nh}^n + p_{nh}' \tag{23}$$

165   The Poisson equation (24) can be discretized into a linear matrix Eq. (25) where the right-hand side

166    $\boldsymbol{B}$ is determined by the divergence of the intermediate velocity field. The adjoint matrix $\boldsymbol{A}$ represents the

167   discrete three-dimensional Laplacian operator with a size of the number of model cells. The specific

168   discrete process for Eq. (24) is introduced in Appendix A.

$$\frac{\partial^2 p_{nh}'}{\partial x^2} + \frac{\partial^2 p_{nh}'}{\partial y^2} + \frac{\partial^2 p_{nh}'}{\partial z^2} = \frac{\rho_c}{\Delta t}\left(\frac{\partial \tilde{u}}{\partial x} + \frac{\partial \tilde{v}}{\partial y} + \frac{\partial \tilde{w}}{\partial z}\right) \tag{24}$$

$$\boldsymbol{A}p_{nh}' = \boldsymbol{B} \tag{25}$$

$$\nabla p_{nh}' \cdot \boldsymbol{n} = 0 \tag{26}$$

169   The proper boundary conditions need to be considered for solving this Poisson equation (24). Here,

170   at the solid boundaries the homogeneous Neumann boundary condition, also called the Zero-gradient

171   condition (26), is used with a good compatibility with the no flux normal to slope, where $\boldsymbol{n}$ is the normal

172   unit vector (Marshall et al., 1997a). Moreover, we assume that nonhydrostatic dynamic processes are

173   weak enough at the sea surface and open boundaries. In other words, the input signals through the

174   boundaries are dominantly hydrostatic with nonhydrostatic pressure perturbation close to zero. More

175   specifically, the nonhydrostatic dynamic framework is restricted in the interior. Hence the Zero-gradient

176   condition is also used at the open boundaries in case of sharp nonhydrostatic pressure gradients. With the

177   above boundary conditions this linear system (25) can be solved via the Krylov subspace method with

178   the PETSc's assistance on parallel computers under the standard MPI-based framework (Balay et al.,

179   2020). It is a highly efficient method devised to precondition the huge and sparse matrix $\boldsymbol{A}$. Here, the

180   multigrid preconditioner (Smith et al., 1996) and flexible generalized minimal residual algorithm (Saad,

181   1993) are employed in numerical validation experiments in this paper to reduce the computational costs.

3. Model applications and assessments

183   Here we present a series of ideal numerical validation experiments to explore the correctness and

184   compatibility of nonhydrostatic algorithms together with the ORCTM. These test cases range from the

185   laboratory-scale cases in a tank to field-scale cases like the northern South China Sea with open

186   boundaries in allusion to the dynamics of ISWs. The first case is the lock-exchange problem as the

187   preliminary validation. The second to fourth cases are designed to explore the nonlinear evolution of

188   ISW caused by its interactions with the changing terrain. The last one is the generated nonlinear internal

189   waves case in a double-ridge environment analogous to the Luzon Strait via boundary tidal forcing,

190   which aims at the generation and disintegration of NIWs to examine the effectivity about open boundary

191   module under the nonhydrostatic algorithms. All test experiments above can demonstrate the capabilities

192   of simulating the evolution of NIWs and ISWs with good compatibility with the nonhydrostatic

193   algorithms.

3.1. The lock-exchange problem

195   When the shear currents flow between the two different density fluids, the Kelvin-Helmholtz

196 instability (hereafter K-H instability) will appear to cause the turbulent diapycnal mixing (Lawrence et

197 al., 1991; Cushman-Roisin, 2005). The perturbation on the interface begins to develop and stimulate

198 gradually numerous eddies with the high wavenumber due to the dispersion. The order of vertical flow

199 magnitude is comparable to the horizontal one so that the nonhydrostatic effect matters from the

200 beginning to the end.
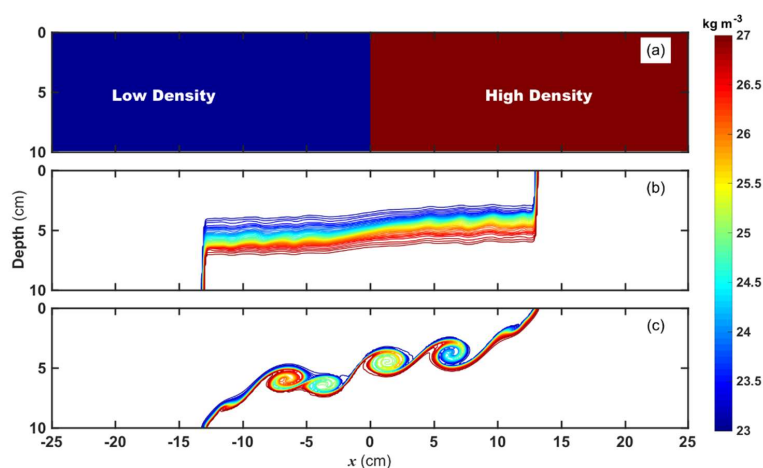
201

202 Figure 1. (a) The initial density ρ' (hereafter the same expression) field of the lock-exchange case, and

203 their contour plots of density at $t = 4.5$ s where the contour interval is 0.1 kg m^{-3} under the hydrostatic

204 (a) and nonhydrostatic (b) framework.

205   We set a rectangle tank separated by a vertical board in the middle at the x-axis origin. Both sides

206 of the tank are separately filled with two different density fluids in Fig. 1a. The gravitational adjustment

207 will proceed when the central board is disengaged just like a lock gate. Here, we refer to the previous

208 configuration as a 2-D problem (Härtel et al., 2000; Fringer et al., 2006; Lai et al., 2010). The horizontal

209 length L is set to 50 cm and the static water height is 10 cm without the topographic change in the tank.

210 And the horizontal and vertical resolution are both 0.001 m. In order to reduce the dissipations out of

211 friction and close to the ideal status, several sensitivity experiments were explored so that the bottom

212 friction coefficient is set to zero and A_{V0} and D_{V0} in formulas (11) and (12) are both set to 2×10^{-6} m^2

213 s^{-1}. The K-H instability process develops rapidly in this configuration with good eddies reconstruction

214 and outstanding waves breaking. Water density averages are calculated based on the prescribed salinity

215 difference on the left and right sides of the tank $\rho_l = 1023.05$ kg m^{-3} and $\rho_r = 1026.95$ kg m^{-3}. The

216 same configuration experiment above but under the hydrostatic balance scheme is also run for

217 comparison. Figures 1b and 1c show the comparison results of density (define $\rho' = \rho - 1000$ kg m^{-3}) at

218 the same time under the hydrostatics and nonhydrostatic balance assumption, which proves that the K-

219 H instability cannot appear resulting from the inapplicability of the hydrostatics balance. The

220 perturbation on the density interface is so tiny that the density fronts cannot develop in the upper and

221 lower layer. To sum up, the mixing caused by the overturning and shear is too weak to be seen. On the

222 contrary, via the nonhydrostatic scheme, the numerous eddies can appear and dissipate energy from the

223 perturbation, mixing the high and low-density water on the interface vigorously. More specifically, the

224 energy is transmitted to the small-scale eddies across the density fronts due to dispersion and nonlinearity.

225 The evolution process of K-H instability is shown in Fig. 2. It is out of gravitational adjustment that

226 the density fronts with heavy water in the bottom and light one in the upper move to the left and right,

227 respectively, causing a velocity shear field and clockwise rotating interface in Fig. 2a. The shear strength

228 gradually increases until breaking the critical point of restoring force that depends on the density gradient.

229 A series of eddies then develop from the middle to both sides of the tank with the turbulent rolling and

230 overturning. They mix the water body with high density at the bottom and upper one with the low density,

231 forming numerous mixing areas in Figs. 2b and 2c. When the bottom density flow is reflected on the wall

232 on the left side, the whole adjustment process begins to develop in reverse of Figs. 2d and 2e, but the

233 strength of subsequent eddies is significantly weakened due to the energy dissipation.
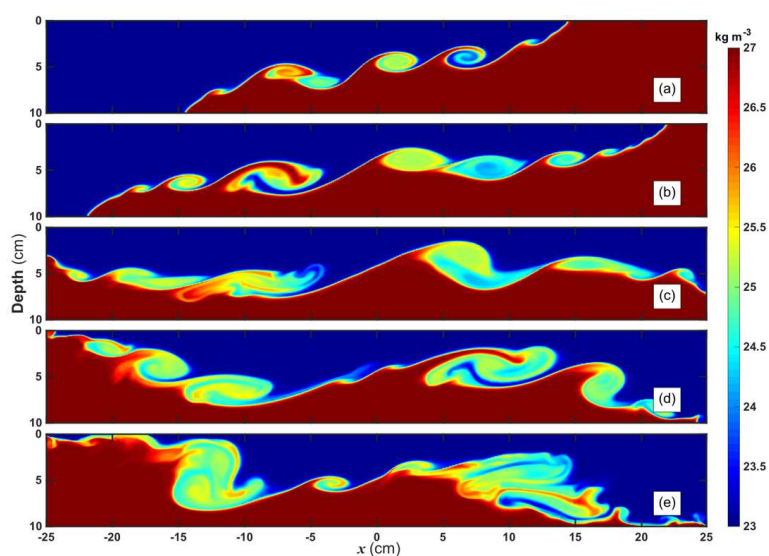
234

235 Figure 2. Density field evolution at t = (a) 5.0, (b) 7.5, (c) 10.0, (d) 12.5, and (e) 15.0 s

236

237   From the density distribution, we can find that the density fronts and eddies processes accompany

238   the gravitational adjustment. In reality, the gravitational potential and kinematical energies (hereafter PE

239   and KE) of the water parcel have been interconverting with total energy dissipating continuously in the

240   tank. KE and PE of the entire tank are obtained from the following formulas.

$$KE = \int\limits_{0}^{L} \int\limits_{-H}^{\zeta} \frac{1}{2}\rho(u^2 + w^2)dxdz \qquad (27)$$

$$PE = \int\limits_{0}^{L} \int\limits_{-H}^{\zeta} \rho gz dxdz \qquad (28)$$

241   Above the formulas ζ is the free surface elevation. The three curves show the fluctuation of PE,

242   KE, and total energy during the K-H instability simulation in Fig. 3. The PE and KE correspond to the

243   maximum and zero due to the initial density distribution and static field in Fig. 3a. Afterward, the PE

244   declines sharply with an opposite change of KE. Both rates of change are almost the same based on the

245   curve slopes, which demonstrate that PE is converted to KE, reaching mutual peaks of about 9.5 s at the

246   end of the first gravitational adjustment. From then on, both of them still maintain the opposite trends

247   with an oscillation of roughly 25 s. In addition, it is worth noting that all kinds of energy show a

248   downward trend with their oscillation time increasing steadily due to the energy dissipations, which

249   seems that their time change rates overall diminish gradually so that KE will drop to zero and PE and

250   total energy (PE+KE) will reach the constant in the end. The results above are similar to the previous

251   works (Harel et al., 2000; Fringer et al., 2006; Lai et al., 2010), implying the correctness of the

252   nonhydrostatic dynamic module.
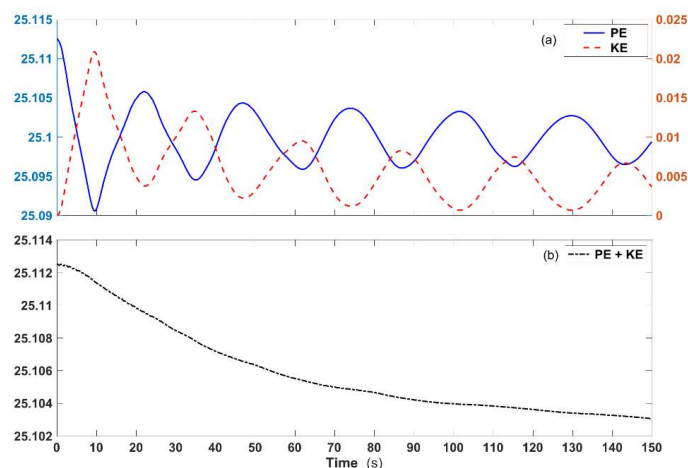
253

254 Figure 3. (a) The timeseries of the kinematical (red dashed line), potential (blue solid line) energy, and

255 (b) the same as total (black dotted line) energy (units: kg m^2 s^{-2}).

3.2. Internal Solitary Wave in a tank

257   Internal Solitary Waves are ubiquitous in the ocean with nonlinear and nonhydrostatic dynamic

258 processes. The laboratory experiments are usually carried out to study the ISWs to make up for the

259 defects of field observations. Additionally, the numerical study in a laboratory-scale experiment also

260 needs to be combined (Grue et al., 2000). We follow the previous experimental configuration (Ma et al.,

261 2019). The tank length is 2.0 m, and the static height is 10 cm without topographic change; The horizontal

262 and vertical resolutions are 2×10^{-3} and 1×10^{-3} m. Here, a gravity collapse method is used to generate the

263 ISW. Specifically, the low- and high-density fluids initially fill the upper and lower layers on the tank

264 with the collapse area on the left side. The collapse height and width are 5.0 cm and 4.0 cm, which will

265 lead to the generation of depression wave type. A schematic diagram of the ISW experiment is given in

266 Fig. 4. Water density averages are calculated in the upper and lower layer with $\rho_1 = 1003.62$ kg m^{-3} and

267 $\rho_2 = 1026.95$ kg m^{-3}. Additionally, the diagnostic module is used to depict the high-frequency variation.

268 The high-frequency outputs are set at points $x = 0.4, 0.8, 1.2,$ and 1.6 m from west to east with an interval

269 of 0.05 s.

270
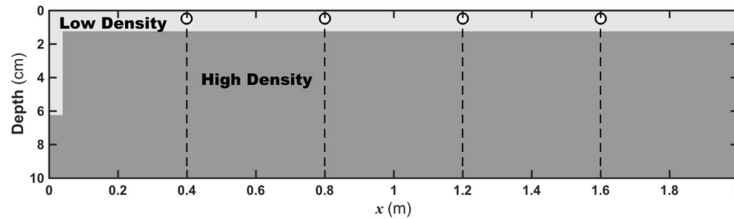
Figure 4. Schematic diagram of ISW case. The dark and light gray indicate the high- and low-density
water, where four white dots refer to the high-frequency output points.

Figure 5 clearly illustrates the evolution of the ISW packet in the tank based on the pycnocline
fluctuation. The isopycnic of 1026 kg m^{-3} can represent the maximum strength of depression waves in
Fig. 5a. The depression wave packet from the west gravity collapse area comprises of the heading wave
and several tail waves with their amplitudes decreasing successively. The heading ISW with the
maximum amplitude propagates faster than the tails behind so that the distance increases between them.
As is exhibited in Table 1 about the heading depression wave characteristics at the four locations, we
find the amplitude of the depression wave with little change and then a slight increase but both no more
than 0.1 cm after $x = 0.8$ m, and the qualitative evaluation of the depression wave speed can be obtained
from the slope of the blue dashed area in Fig. 5b. Because the ISW packets are still at the stage of gravity
adjustment before arriving at $x = 0.2$ m, then wave speed increases slowly after $x = 0.2$ m but with its
increment less than 0.01 m s^{-1}. The above indicates that the internal solitary wave from gravity collapse
can propagate to the east steadily in our simulation. Besides, the characteristic westward reflected waves
(the blue line in Fig. 5a) with the larger amplitude prove that the wave-wave interactions happen between
the reflected and starting tail waves.

287
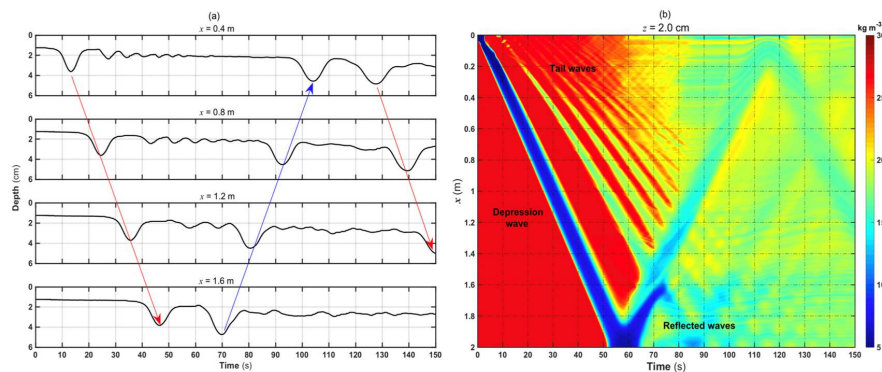
Figure 5. (a) The density timeseries of 1026 kg m^{-3} at the four high-frequency output locations from the

289   west to east. The left red and blue arrow lines indicate the eastward and westward waves, and the right

290   red means the eastward reflected waves from the channel start. (b) Hovmöller diagram showing the

291   density at $z = 2.0$ cm where the time interval is 0.1 s.

292

293   Table 1 The characteristics of the depression heading wave at the four points

location (x/cm) parameters	0.4	0.8	1.2	1.6
amplitude (a/cm)	2.369	2.362	2.392	2.469
characteristic wavelength (L/cm)	19.632	21.643	23.206	25.822
nonlinearity (ε)	0.237	0.236	0.239	0.250
dispersion (μ)	0.259	0.213	0.186	0.150

294
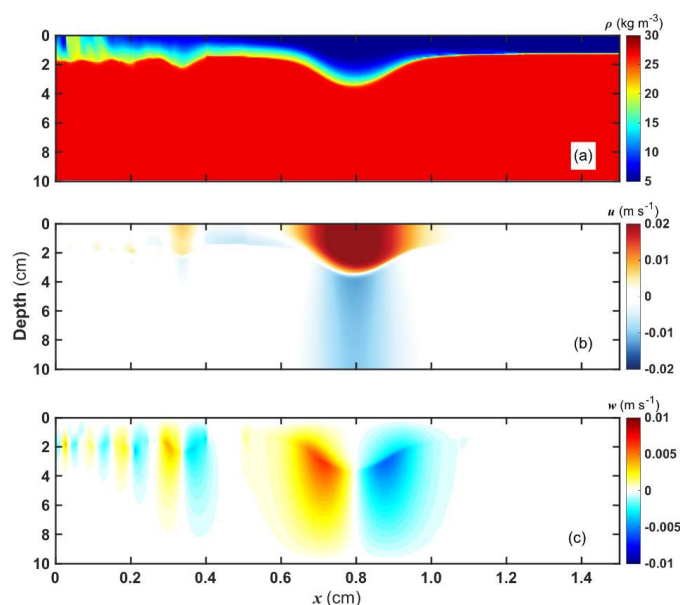
295

296   Figure 6. From top to bottom, density, horizontal and vertical velocity fields of the ISWs at $t = 24.5$ s.

297

298   We select a snapshot result for verification when the heading wave arrives at $x = 0.8$ m shown in

299   Fig. 6. The strongest horizontal velocity of the depression wave is 0.023 m s^{-1}, and the vertical flow can

300   reach up to 0.0065 m s^{-1}. The characteristic velocity fields are in line with the clockwise structure of a

301   theoretical depression internal solitary wave. Furthermore, the nonlinearity $\varepsilon = a/h$ and dispersion

302    $\mu = (h/\lambda)^2$ are calculated at the different locations in Table 1, where a, h, and λ are the amplitude,

303   water height, and characteristic wavelength, and the KdV model (Benjamin, 1966) described in Appendix

304   B is used to calculate theoretical waveforms at the four locations depicted in Fig. 7. The comparison

305   demonstrates that the results are more consistent with the KdV model than m-KdV model. According to

306   the nonlinearity ε from Michallet and Barthélemy (1998), the small and large-amplitude ISW can be

307   classified when $\varepsilon < 0.05$ and $\varepsilon > 0.05$, respectively. Whereas the application of the KdV model

308   requires a balance between the weak nonlinearities and dispersion (Ono, 1975), namely, assuming

309   that $\mu = O(\varepsilon) \ll 1$. Despite the large-amplitude waves simulated from our model with $\varepsilon > 0.05$, the

310   nonlinearity and dispersion are of the same order and small enough that the heading wave can be deemed

311   under weak nonlinearity, which is why their waveforms are better described well by the KdV model.

312   Therefore, the analysis results indicate that the simulated internal solitary wave is close to the KdV theory

313   and can be performed accurately via our nonhydrostatic model.
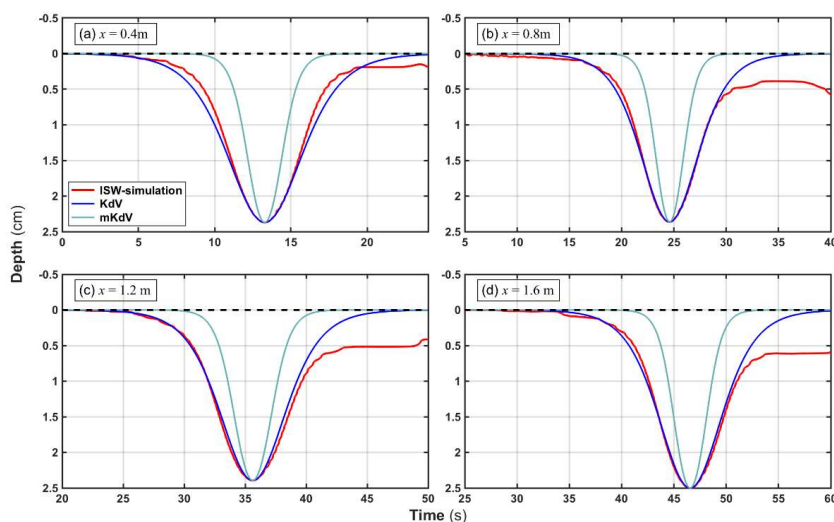
314

315   Figure 7. The interface displacement induced by ISW at four high-frequency output locations. The red

316   lines indicate the 1026 kg m^{-3} isopycnic, and the blue and cyan lines represent the KdV and m-KdV

317   model results.

318   **3.3. Internal Solitary Wave shoaling on a Gaussian terrain**

319   Based on the experiment configuration in section 3.2 (also called Exp. 3.2). Here, a slowly varying

320   terrain is implemented to explore the nonlinear evolution of internal solitary wave, especially the wave

321   shoaling. As shown in Fig. 8, the left half of the Gaussian curve is reserved as the slope-shelf terrain

322 starting between x = 1.0 and 1.3 m with the height of 5.0 cm, and then the water depth remains unchanged

323 from x = 1.3 to 2.0 m corresponding to the shallow water zone. The high-frequency outputs are acquired

324 during the climbing process of ISWs at points x = 0.4, 0.8, 1.0, 1.2, 1.3, 1.4, 1.6, and 1.8 m from the west

325 to east with the output same interval as Exp. 3.2.
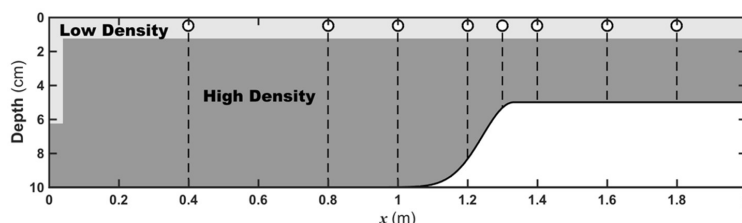
326

327 Figure 8. As in Figure 4, but with half-Gaussian topography in the east of the tank, where eight white

328 dots refer to the high-frequency output points.

329 Figure 9 reveals the evolution of the internal solitary waves with varying topography. The heading

330 ISW holds a stable packet at x = 0.4 m and begins to shoal after reaching the position of 1.0 m. Afterward,

331 its bottom velocity firstly experiences the topographic change, resulting in the different wave front and

332 rear effects. Specifically, the speed of wave trough is less than the rear, contributing to the wave front

333 gentle sloping but wave rear gradual steepening, which shows a similarity with Vlasenko et al. (2002).

334 Then the closed isopycnic contour mirrors the overturning and rolling due to the wave breaking in the

335 rear at x = 1.2 m in Fig. 9a. Apart from the overall wave breaking process above, it is also found in Fig.

336 9b that the reflected waves propagate to the west at x = 1.2 m due to the terrain shoaling. In other words,

337 the wave breaking and refection both lead to the depression wave energy being attenuated substantially.

338 When arriving at the east of x =1.2 m, the original depression wave past the critical point so that an

339 elevation wave springs up in the wave rear, where the upper layer is thicker than the lower one in Fig.

340 10a. Then the elevation wave continues to propagate eastward. The high-density water accumulates the

341 upper water increasingly on the right wall, forming a collapse area between x = 1.8 m and the east wall,

342 where the thickness of the upper layer is larger than lower layer. Ultimately, the reflected waves including

343 a series of elevation tail waves, are released at x = 1.6 m. In detail, the first elevation is the leading one

344 with the rank-ordered structure in the rear all propagating to the west. After reaching the deep-water zone

345 left to 1.3 m, the wave rear begins to steepen and sink, generating a depression wave behind it. Namely,

346 the soliton wave passes the critical point inversely as a consequence of the water deepening.
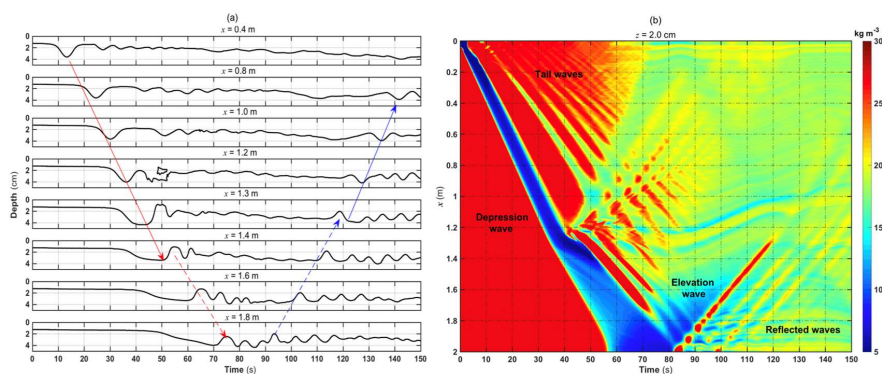
Figure 9. As in Figure 5, (a) the solid and dashed arrow lines indicate the depression and elevation waves, and the red and blue mean the starting westward and reflected eastward waves. (b) Hovmöller diagram showing the density at $z = 2.0$ cm.

For the sake of further exploration of the evolution of depression wave, the distributions of the vorticity ($\zeta = \partial w/\partial x - \partial u/\partial z$) with velocity vector are displayed in Fig.10. The soliton features a depression corresponding to negative vorticity with an anticyclonic structure before reaching the shelf topography. And then, the vertical shear increases rapidly and strengthens the positive vorticity at the bottom when the ISW closes to the top of the slope in Figs. 10a and 10b. As a consequence of shoaling, the backward overturning springs up between $x = 1.2$ and 1.3 m, marking the ISW entering the breaking instability stage (Helfrich and Melville, 1986). At this time, even though wave breaking and reflection cause the wave energy dissipation partially, the fraction of the depression wave can reach the shallow water zone, leaving behind a cyclonic vortex above the slope-shelf in Fig. 10c. This partial soliton wave is adjusted quickly when the thickness of the upper layer is more significant than the lower's in the light of the boundary of the negative vorticity area in Fig. 10d. As a result, the elevation wave begins to emerge at the back of the original wave, corresponding to the positive vorticity with a cyclonic structure when the reverse situation occurs. Notably, the vortex from the breaking of the depression wave weakens slowly and motivates the small-scale waves with high wavenumber propagating to both sides in Figs. 10e and 10f, which is consistent with the propagation characteristics of the reflected waves near $x = 1.2$ m in Fig. 9b.

367
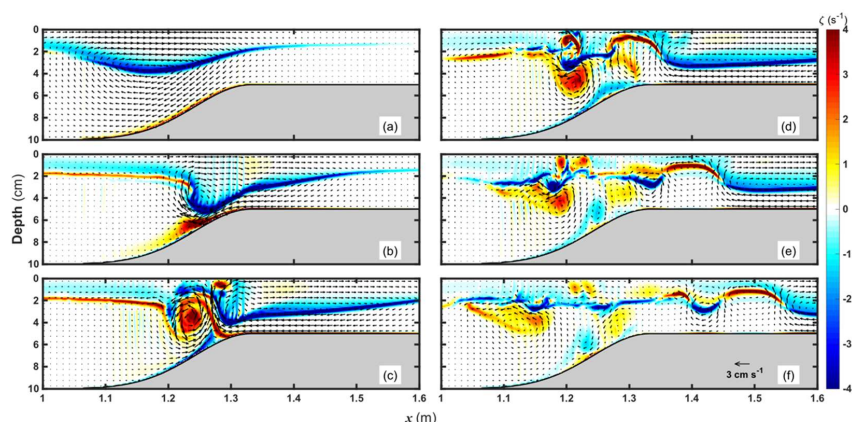
Figure 10. The shoaling of a depression soliton where the velocity fields (black arrow) and the vorticity results

(color) are shown at t = (a) 35, (b) 40, (c) 45, (d) 50, (e) 55, and (f) 60 s.

It is also worthy of highlighting the evolution of the reflected eastward waves. We also visualize

the process of the second reverse situation due to the wave deepening in Fig. 11. It can be seen that there

is a strong elevation wave at x = 1.4 m propagating to the deep-water zone with the crest corresponding

to positive vorticity, followed by a series of rank-order waves showing a sinusoidal variation. Particularly,

the wave train can be considered linear approximatively based on the alternated positive and negative

vorticity with the water interface almost located in the middle layer. The nonlinear parameter α in the

wave train region is close to zero in terms of the KdV model. As the depth becomes deeper, the crest of

the elevation wave gradually grows down and flattens with the wave rear sinking. The original elevation

cannot be maintained in the deep water, transforming into a depression wave with the velocity fields

adjusted accordingly.
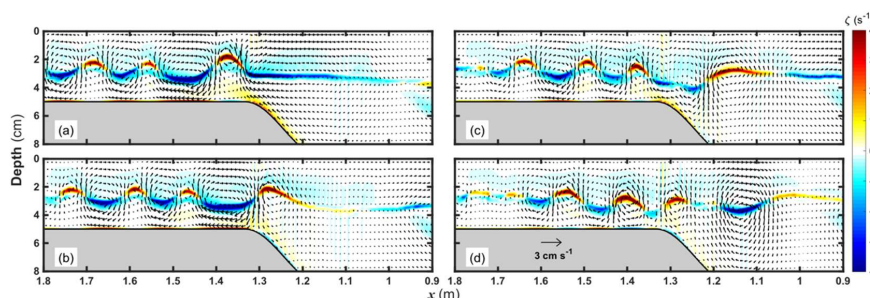
Figure 11. As in Figure 10, the elevation wave propagates westward to the deep water where the x-axis is inverse

for convenience at t = (a) 115, (b) 120, (c) 125, and (d) 130 s.

384   Because the ISW in the adjustment stage is not stable enough to coincide with the KdV model after

385   pasting the critical point, we select the two types soliton results for verification before the reverse

386   situation occurs. The comparison between theoretical and numerical results is shown in Fig. 12 at $x = 0.8$

387   and 1.4 m before the wave shoaling and descending, respectively. We can find that the depression

388   waveform conforms to the KdV model results before climbing the slope, whereas the elevation is close

389   to the m-KdV model. Compared with the position of $x = 0.8$ m with $\varepsilon = 0.233$, a stronger nonlinearity

390    $\varepsilon = 0.331$ at $x = 1.4$ m in the shallow water could be the result of interaction between the ISW and the

391   varying topography. Actually, a larger ratio of amplitude in the shallow water proves results closer to the

392   m-KdV theory, which compares well with the conclusions of Michallet and Barthélemy (1998) in a

393   satisfactory way.
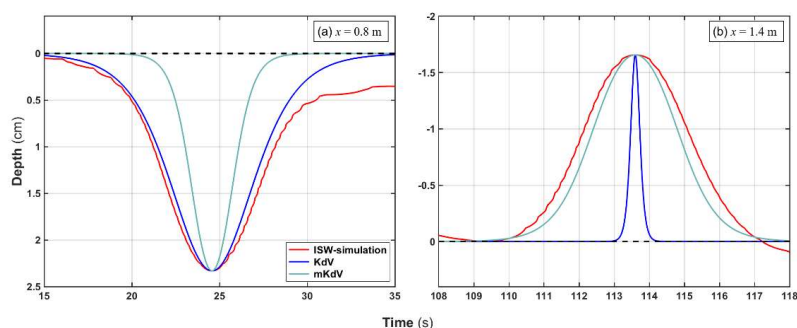
394

395   Figure 12. Wave profiles at $x = 0.8$ (a) and 1.4 m (b). The left refers to the depression heading wave

396   before shoaling and the right is the reflected elevation heading wave in the shallow water, which both

397   are plotted in red line, while and the blue and cyan lines represent the KdV and m-KdV model results.

398   **3.4. Internal Solitary Wave breaking on a slope.**

399   To further characterize a complete breaking and dissipative process of ISWs due to wave climbing,

400   we set a linear slope identical to Michallet and Ivey (1999). As is shown in Fig. 13, the tank length is 2.0

401   m; The height is 15 cm with the linear terrain placed on the east side. The depression wave is to be

402   dissipated due to increasing bottom friction at the shelf break. The spatial resolution is the same as Exp.

403   3.2, which can ensure the same timestep according to Courant-Friedrichs-Lewy (CFL) condition. In

404   addition, to compare with Bourgault and Kelley (2004) model results, water density averages are

405   calculated to be $\rho_1 = 1000.01$ kg m^{-3} and $\rho_2 = 1047.00$ kg m^{-3} in the upper and lower layers. Via several

406 sensitivity experiments about collapse area, the amplitude of depression wave can reach approximately

407 2.8 cm when the collapse height is 9.0 cm with its width same as Exp. 3.2. Although the stimulated wave

408 strength is slightly greater than the results from Bourgault and Kelley (2004) due to the different wave

409 generation methods, it is predictable that the breaking of the larger-amplitude ISW will be more dramatic

410 with a prominent performance for model verification.
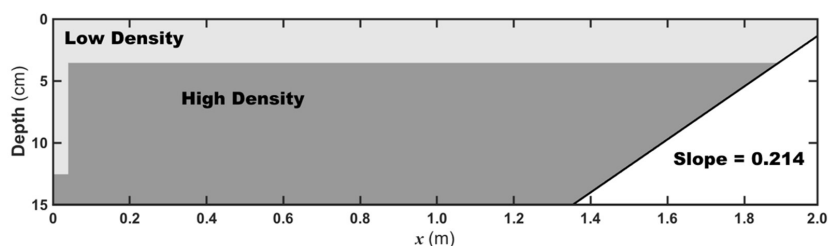
411

412 Figure 13. As in Figure 4, but with a linear slope terrain in the east of the tank and related configuration

413 is referred by Bourgault and Kelley (2004)

414 The corresponding density and velocity fields produced by the depression soliton are presented in

415 Fig. 14 at this moment before wave shoaling. The horizontal velocity induced is about 3.0 cm s^{-1} at the

416 surface and varies up to 3.5 cm s^{-1} at the core of the wave trough. Meanwhile, the vertical velocity

417 distribution presents a double-core structure reaching $\pm$0.8 cm s^{-1}. The unique anticyclonic velocity

418 characteristic is entirely consistent with the experimental results of Bourgault and Kelley (2004). We

419 select the four different times with the evolution of wave shoaling illustrated in Fig. 15. In addition to

420 wave breaking accompanied by the waveform steepening in the rear, a significant density fronts rolling

421 in the wave front evolves along the linear slope during the overall shoaling process in Figs. 15a and 15b.

422 Specifically, while the depression wave continues getting closer to the shallow zone, the effect of bottom

423 friction can maintain a vertical shear with the potential energy increasing. Then the wave-induced

424 diapycnal flow contributes to high-density water under the interface transported continuously to the

425 shallow zone right to the slope in Fig. 15c, which intensifies the diapycnal mixing and dissipation on the

426 density interface. On the other hand, there is another pronounced change in Fig. 15d compared to the

427 experiment in Exp. 3.2. A few small-scale eddies emerge along with the sheared interface in density

428 fronts on account of the shear instability but are dissipated promptly via turbulent viscosity.
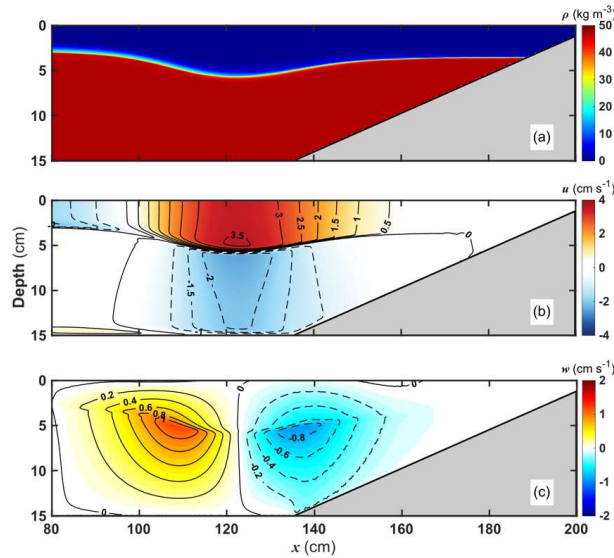
Figure 14. As in Figure 6, but with the time referring to $t = 15$ s before the wave shoaling.
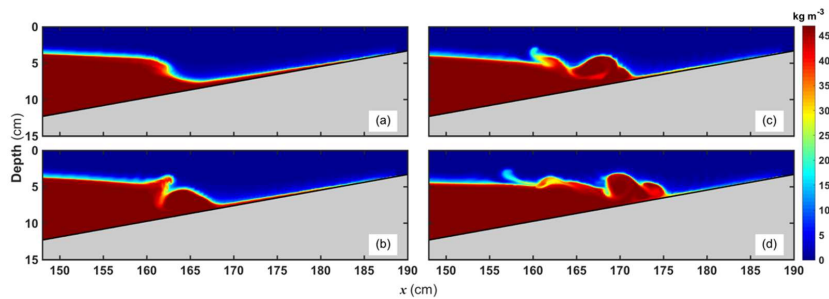
Figure 15. Wave breaking with density front rolling at $t =$ (a) 22, (b) 23, (c) 24, and (d) 25 s.

We compare the velocity field distributions with the observation results via PIV technology from Michallet and Ivey (1999) and nonhydrostatic numerical experiments from Bourgault and Kelley (2004) in Fig. 16 to further evaluate and validate the wave breaking process. Accordingly, when the depression wave arrives over the slope, its depression waveform and anticyclonic flow field are modulated by the topographic shoaling to flatten the wave front and enhance the current down the slope. Meanwhile, the smaller cyclonic eddy appears and clings to the slope under the steepen wave rear. Furthermore, as the depression wave continues shoaling, the cyclonic eddy strengthens and expands its scope of influence, resulting in a strong overturning from near the bottom layer to promote the wave steepening, which presents a good agreement with the results from Sect. 3.3. We also found that the anticyclonic flow field persists in weakening as an effect of bottom friction. In contrast, the scope of the

443   cyclonic eddy expands and moves the shallow zone with the waveform distorted furtherly. In general, all

444   the above nonlinear processes are similar to the previous laboratory and model results. Our

445   nonhydrostatic model can also resolve the nonlinear evolution of the internal solitary waves at shelf break

446   with a high accuracy.

447
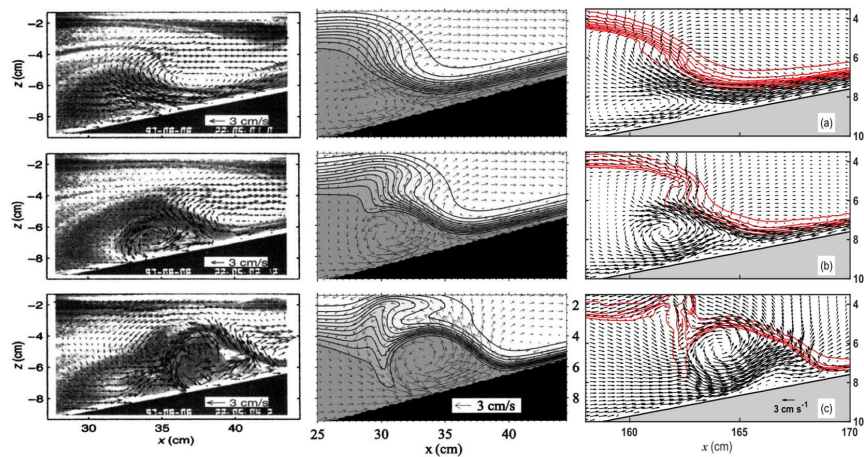
448

449   Figure 16. Comparison of velocity fields during the wave breaking on a linear slope between (left) the

450   PIV observations in the laboratory (Michallet and Ivey, 1999), (middle) the numerical model simulation

451   (Bourgault and Kelley, 2004), and (right) the ORCTM simulation at t = (a) 21.7, (b) 22.2, and (c) 23.2 s

452   from top to bottom. The red contours indicate the isopycnic lines.

453

3.5. Nonlinear Internal Waves in a double-ridge system

The last validation experiment is to examine the generated nonlinear internal waves via tidal flow over the varying topography. We set up an underwater double-ridge system comparable to the Luzon Strait in the northern South China Sea. Meanwhile, this validation case is considered to be a 2-D problem for the reduction of computational costs. The topography in this double-ridge system is fitted approximately with the Gaussian function given as

$$H(x) = 3000 - h_w \times exp\left(-\left(\frac{x - x_w}{20 \times 10^3}\right)^2\right) - h_e \times exp\left(-\left(\frac{x - x_e}{20 \times 10^3}\right)^2\right) \qquad (29)$$

In Eq. (29), $H(x)$ is the water depth; the height of the East and West Ridge (h_e and h_w) is 2500 and 1300 m in sequence with an interval and widths of 100 km, which is similar to the real topographic characteristics in the Luzon Strait. As shown in Fig. 17a, the static water height is 3000 m, where the East and West Ridge (hereafter ER and WR) are located at the coordinate origin and $x = $ -100 km; the horizontal and vertical grid resolutions are 200 m and 10 m. Besides, to simplify the background environment and get closer to the natural wave source fields, we use the horizontally uniform stratification as the initial field to drive our model. Here, the reprehensive stratification in Figs. 17b to 17d stems from the summer stratification in 2011 of GLORYS12V1 reanalysis product in CMEMS (Copernicus Marine Environment Monitoring Service) as the spatial mean around the source of generated ISWs in the Luzon Strait, since the large-amplitude ISWs are observed during the same period on the SCS continental shelf and the strong thermocline structure in summer is usually conducive to the formation of baroclinic tides in the Luzon Strait (Zheng et al., 2007; Buijsman et al., 2010b; Ramp et al., 2019). As for the tidal categories, owing to the generation of the semidiurnal internal tide with the modulation of the diurnal one (Buijsman et al., 2010a; Zeng et al., 2019) in the Luzon Strait, we define the M_2 and K_1 tidal currents amplitudes as 5.0 and 4.0 cm s^{-1} corresponding to the semidiurnal and diurnal components at the two open boundaries whose sponge thicknesses are both approximately 40 km. Additionally, the slope criticality γ (Gilbert and Garrett, 1989; Shaw et al., 2009) no less than one is usually essential with the formation of linear internal waves.

$$\gamma = \frac{dH}{dx} \bigg/ \sqrt{\frac{\omega^2 - f^2}{N^2 - \omega^2}} \qquad (30)$$

in which ω is the tidal angular frequency; N^2 is the buoyancy frequency squared; f is zero without regard to rotation. Around the East Ridge γ is larger than unity regardless of the M_2 and K_1 tide with

480   the supercritical topography. Therefore, it is predictable to generate the internal waves due to the

481   interactions with barotropic flow over the East Ridge. We run the model for 10 days from initial static

482   fields. The diagnostic module is also used to depict the high-frequency variation with the output interval

483   of 1 min at x = -250, -350 km.
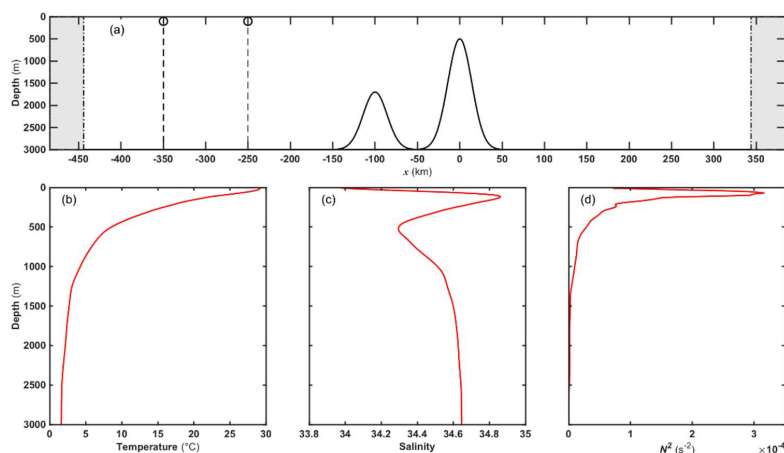
484

485   Figure 17. (a) The sketch of generated NIWs over the submerged double-ridge system case, and the

486   gray zones indicate the sponger layers. The summer stratification in 2011 including (b) temperature, (c)

487   salinity, and (d) buoyancy frequency squared are from the spatial mean within 20.25 °N–20.85 °N,

488   121.7 °E–122.08 °E corresponding to the source of internal waves in the Luzon Strait (Zhang et al.,

489   2011).

490
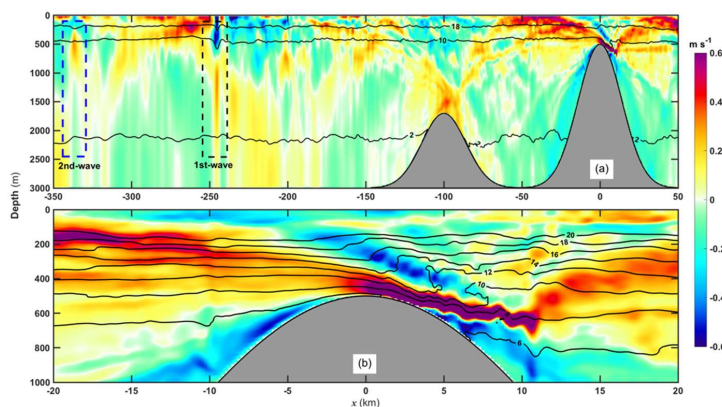
491

492   Figure 18. Distributions of horizontal baroclinic velocity with the temperature (°C) contours for

493   western far-field (a) and source field (b) when the maximum eastward tidal current at East Ridge

494   reaches the end of ebb on the sixth day, where the blue (black) dashed box means the 2nd mode (1st

495   mode) ISW packets.

496   Figure 18 shows the maps of horizontal baroclinic velocity $u' = u - U$ where u is the total

497   velocity and U is the barotropic flow velocity. From the characteristics of the source field, it is found

498   that the generation of internal tide beam propagating eastward and westward centered from the eastern

499   side of East Ridge. The eastward barotropic flooding current flows continuously over the east ridge with

500   the maximum barotropic current up to 0.0531 m s^{-1}. The hydraulic jump can appear with the isotherms

501   fluctuation up to roughly 200 m on the eastern side, which indicates the formation of Lee waves to a

502   certain extent. Above internal waves generation due to tide-topography interactions can be described

503   with several non-dimensional parameters at the source: (1) the tidal excursion parameter $\varepsilon = U_0/L\omega$,

504   which can be associated with the generation of internal beam under the critical or super-critical

505   topography where U_0 is barotropic current amplitude from the far-field and L is the characteristic

506   length for topography (Garret and Kunze, 2007, Chen et al., 2017). (2) the Froude number $Fr = U/c$,

507   and the topographic form $Fr_z = \omega/N(dH/dx)$, in which c is the mode-1 linear speed for the

508   eigenvalue problem (Legg and Adcroft, 2003; see Appendix B). Specifically, Legg and Klymak (2008)

509   found that the nonlinear hydraulic jump will develop with lee waves generation when $Fr_z < 1/3$.

510   Moreover, it is worth paying attention to the tidal excursion far less than unity that agrees with the

511   formation of the linear internal beam on the critical or super-critical topography but cannot ensure the

512   appearance of the Lee waves altogether. For instance, the Lee waves remain strong in the Luzon Strait

513   despite the tidal excursion under the unity ($\varepsilon \approx 0.4$) in previous model results (Buijsman et al., 2010b).

514   the tidal excursion parameter ε and the Froude number Fr in our model are calculated to be 0.025 and

515   0.018, indicating the generation of multi-modal baroclinic tides and upstream propagation of internal

516   waves with the sub-critical barotropic current over the east ridge. Furthermore, the maximum

517   topographic Froude number is just 0.3362 around the East ridge with the approach to the regime transition

518   value 1/3, which ensures that the nonlinear hydraulic jump can develop with Lee waves on the east of

519   East ridge, which helps to explain well the evolutions of the internal beam and hydraulic jump in our

520   simulation and confirms to the mixed tidal lee wave regime in the Luzon Strait (Chen et al., 2017).

521
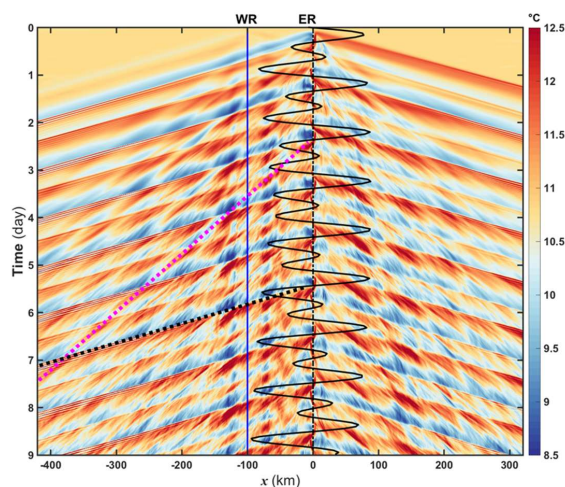
Figure 19. Hovmöller diagram about the global temperature timeseries at z = 400 m, where the time

interval is 15 mins. The black solid curve indicates the tidal current at the East Ridge, and the blue

solid line means the west ridge location. The black and magenta dashed lines are the first and second-

mode Internal Solitary Waves.

The westward internal tide beam emitted from the East Ridge reaches the sea surface and reflects

back into the deep sea, and the internal tide beam can propagate to the top of the West ridge below 1500

m depth and reflect back to the upper layer again. Between the double ridges such a more significant

portion of beam energy captured by the waveguide in the pycnocline can strengthen the upstream

influence to propagate horizontally westward in Fig. 18b, which can trace back to the source of the

internal solitary wave packets of the far-field. However, the strong dissipation for the high modal internal

waves contributes to the vanishing of the internal beam structure and allows the nonlinear evolution of

low-mode baroclinic tides. The significant internal solitary wave packets can appear and propagate

westward from -150 km, marking the disintegration of the nonlinear internal waves energy. Specifically,

the first-mode ISW packet emerges from x = -250 to -200 km. Meanwhile, the second-mode ISW

between x = -350 and -300 km performs the convex wave packet. We can achieve the propagation

characteristics of these ISWs via analyzing the global temperature timeseries at 400 m water depth layer

illustrated in Fig. 19. The second-mode ISW propagates slower and weaker than the first-mode wave

packet. Besides, it can be distinguished that the two first-mode wave packets can propagate westward,

one of which is stronger with the structure of several tail waves, and the other is almost solitary and weak,

symbolizing the observed changes in the structure and timing of type-a and b waves (hereafter a-wave

542   and b-wave) originating from the Luzon Strait (Ramp et al., 2004; 2019; Zhao and Alford, 2006). The

543   relatively weak second-mode concave wave can be found distinctly following the a-wave from the west

544   of -300 km. To sum up, our multi-modal baroclinic tide structures originating from the double-ridge

545   system can propagate to the far-field and the low-mode internal waves gradually perform the

546   corresponding ISWs due to the nonlinear enhancement, which shows a good agreement with the other

547   two-dimensional experimental results (Buijsman et al., 2010a; 2010b; Vlasenko et al., 2010).
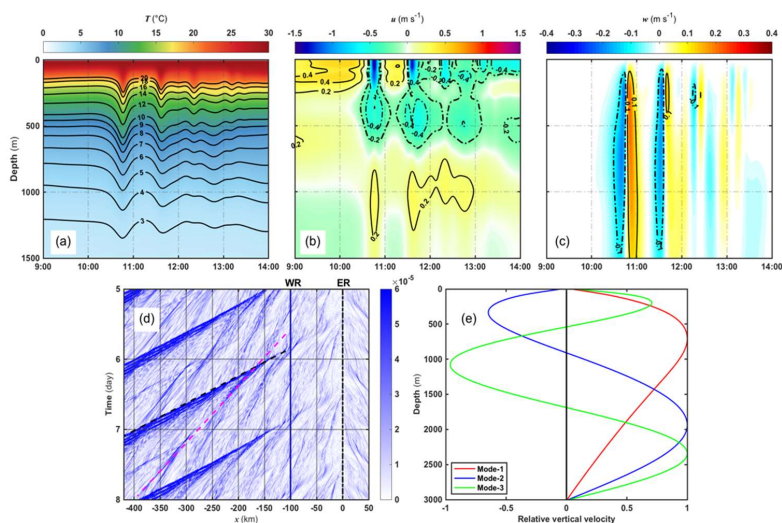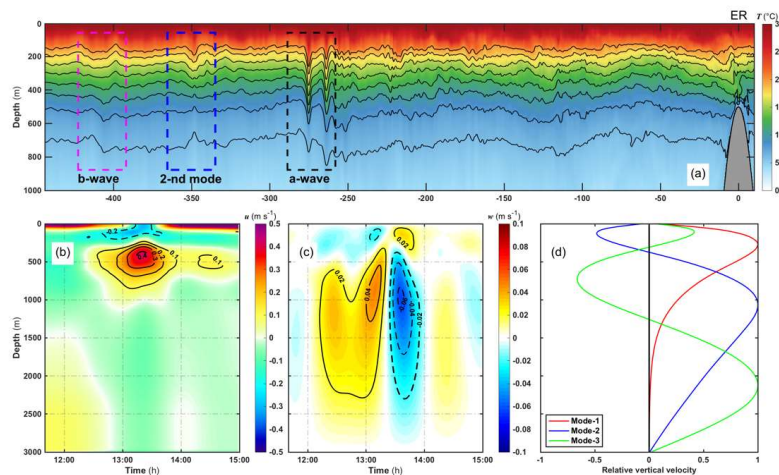

549   Figure 20. (a) The temperature (°C), (b) horizontal baroclinic velocity (m s^{-1}), (c), and vertical velocity

550   (m s^{-1}) structures of the first-mode ISW packet at x = -250 km on the sixth day. (d) The SSHG

551   Hovmöller diagram during the corresponding period where the black and magenta dashed lines indicate

552   the first and second-mode ISW packets. (e) The normal mode profiles of vertical velocity for the first

553   three modes via the Taylor-Goldstein equation.

554   To evaluate the comparison between the numerical ISWs with internal wave theory, we choose the

555   results of the first-mode ISW at x = -250 km shown in Fig. 20. It is found that a first-mode ISW packet

556   including three tail waves arrives at the position after 10 a.m. on the 6th day. The maximum fluctuation

557   of the first-mode ISW packet can reach 206 m between 650 and 900 m water depths. The westward

558   horizontal baroclinic velocity associated with the wave packet prevails above 200 m with the maximum

559   strength of roughly 1.41 m s^{-1}, and the corresponding downwelling region is located between 200 and

560   1500 m with the strongest downward velocity up to 0.22 m s^{-1}. According to the Sea Surface Height

561   Gradient (SSHG, SSHG is defined $\sqrt{(\nabla \zeta)^2}$), the average propagation speed of this wave packet is

562   approximately 3.17 m s^{-1} based on the slope of SSHG contour. Moreover, we solved the Taylor-Goldstein

563   equation (Miles, 1961; Liu, 2010; see Appendix B) at 10 minutes before this wave packet reached x =

564   -250 km. The normal mode of vertical velocity is subject to the rigid-lib boundary condition illustrated

565   in Fig. 20e. it is found that the location corresponding to the maximum modal function is 710 m in

566   agreement with the model results. However, the propagation speed is greater than the first-mode linear

567   result of 2.69 m s^{-1}, which might be probably attributed to the linear theory with the underestimated effect.

568   Therefore, The KdV model is also used to analyze the depression wave, which shows that the dispersion

569   parameter β is 2.4×10^5 m^3 s^{-1}, and the nonlinear parameter α = -3.4×10^{-3} s^{-1} denotes that the predicted

570   depression wave is consistent with the simulated results (Helfrich and Melville, 1986). Nevertheless, the

571   theoretical nonlinear velocity of about 2.88 m s^{-1} is slightly lower than the realistic propagation velocity

572   obtained from the simulated results. It is probable that the increasing nonlinearity with the steepening of

573   internal tides ultimately leads to the larger propagation speed of this first-mode ISW packet.

574

575   Figure 21. (a) The temperature (°C) field from the west side of East Ridge at 13:00 on the seventh day,

576   where dashed rectangles refer to the respective type waves. (b) The horizontal baroclinic velocity (m s^{-1}

577   ^{1}) and (c) vertical velocity (m s^{-1}) structures of the second-mode ISW at x = -350 km in the meantime.

578   (d) The normal mode profiles about vertical velocity for the first three modes via the Taylor-Goldstein

579   equation.

580   It is also noticeable that the multi-modal structure of baroclinic tides generated from the double-

581   ridge system can evolve into the high-mode internal solitary waves due to the nonlinear enhancement.

582   We can recognize clearly the distinct ISW packets from the isotherm displacement that refers to the type-

583   a, second-mode, and type-b waves from the source to the far-field in Fig. 21a. The a-wave packet features

584   the most substantial strength with tail waves when its vertical excursion induced by the heading wave

585   can reach up to 120 m. In contrast, the weaker b-wave contains one solitary depression wave in the west

586   to x = -400 km. They both originate from multi-modal internal tide caused by the tide-topography

587   interactions in the double-ridge system, but the b-wave is more associated with the west ridge (Buijsman

588   et al., 2010a; Zeng et al., 2019). Between a- and b-wave, there is a second-mode ISW packet classified

589   obviously as a structure of concave wave whose upper and lower isotherm is toward downward and

590   upward. The isotherm fluctuation can reach up to -57.2 and 140.6 m in the upper and lower layers

591   referring to the rough depths of 180 and 1000 m. Based on the slope in Fig. 21d, the propagation speed

592   of this second-mode ISW signal is about 1.36 m s^{-1}. It is predictable that the a-wave packet will follow

593   the second-mode signal due to the larger speed. Namely, the first and second mode solitary waves as the

594   leading carriers transferring energy from the source to far-fields until dissipating thoroughly. The multi-

595   modal solitary waves field agrees with the previous two-ridge experimental results via the MITgcm

596   (Vlasenko et al., 2010), which indicates that the multi-modal baroclinic tides propagate westward with

597   the low-mode signals evolving into the ISWs.

598   The second-mode ISW packet with corresponding velocity fields timeseries at x = -350 km are

599   shown in Figs. 21b and 21c. The horizontal baroclinic velocity field has a sandwich-shaped vertical

600   structure, and the maximum 0.42 m s^{-1} is located in the middle layer between 200 and 600 m.

601   Nevertheless, the baroclinic velocity above 200 m is distinct from the first-mode ISW packet with a small

602   value of 0.2 m s^{-1}. Additionally, a double-peak structure performs and is distributed at the depths of 150

603   and 1000 m from the vertical velocity field where the strength in the deep layer is stronger than the

604   upper's, resulting in the smaller isotherm fluctuation above 200 m. Here, the Taylor-Goldstein equation

605   is also used to acquire the eigenfunction about the vertical velocity shown in Fig. 21d. The second-mode

606   eigenvalues have two peaks in vertical direction whose depths correspond to 150 and 1070 m with the

607   latter strength stronger than the former, and the corresponding phase speed is about 1.34 m s^{-1}. The above

608   theoretical results can compare well with the distribution of stimulated characteristics, indicating that our

609   nonhydrostatic ocean model succeeds in describing the nonlinear evolution of higher modal baroclinic

610   tides.

611   **4. Conclusion**

612   In this paper, a reliable ocean model called ORCTM which is able to reproduce nonhydrostatic

613   dynamics with the marched open boundary condition to depict the evolution of the internal solitary waves,

614   is introduced. Based on the fractional step method, the three-dimensional fully nonlinear momentum

615   equations are involved and considered thoroughly under the Boussinesq fluid. It is needed to solve the

616   three-dimensional Poisson equation subject to different boundary conditions before the pressure

617   correction method is employed to acquire the velocity field corrected via nonhydrostatic pressure

618   gradients at the new timestep. In order to match the nonhydrostatic algorithm and realize larger-amplitude

619   ISWs simulation in an ocean-scale case, an exponential relaxation term is implemented to the control

620   equations through the sponge layers as the open boundary condition.

621   A series of two-dimensional ideal numerical experiments corresponding to the nonlinear evolution

622   of the internal solitary waves and baroclinic tides are designed to verify the nonhydrostatic module. Here,

623   the results of the validation experiments can be in accord with the theoretical framework of the

624   nonhydrostatic dynamics and demonstrate that the ORCTM can successfully reproduce the generation,

625   propagation, and dissipation of Internal Solitary Waves in laboratory-scale cases. Specifically, the reverse

626   situation due to wave shoaling and deepening can be compared well to the previous simulation when

627   considering the topographic change. Meanwhile, the ORCTM can capture the density fronts with the

628   cyclonic eddy induced by the wave breaking, which shows enough accuracy with a good stability.

629   Notably, the multi-modal structure of baroclinic tides stems from the tide-topography interactions

630   in the double-ridge system based on the real topographic features in the Luzon Strait of the northern

631   South China Sea, where the largest internal solitary waves in the world can exist. This application of this

632   case suggests that our model can reproduce the life cycle of ISWs induced from the Luzon Strait and

633   capture the whole alternation process of type-a and b internal solitary wave packets. The first two mode

634   ISWs structure compares well to those derived from the internal wave theoretical model.

635   Compared to the in-situ observations, the simulation of internal waves can mirror the macroscopic

636   structure and assist with the implementation of observations. However, the predictability of nonlinear

637   internal waves characteristics relies on the model performance and reliable external conditions such as,

638   the realistic stratification, bathymetry, and background circulation. Enhancing the fidelity of ISWs

639   remains to be challengeable. Nevertheless, it can be concluded that this regional nonhydrostatic ocean

Geoscientific Model Development Discussions

640 model can provide a choice for the oceanography scientists who are interested in internal waves research

641 and internal waves numerically prediction.

642

643 **Appendix A**

644 **Discretization Algorithms of the Poisson Equation**

645   According to the idea of fractional steps (Chorin,1968; Press et al., 1988), a pressure correct method

646 considering the nonhydrostatic component is employed to calculate the intermediate velocity over the

647 original hydrostatic balance scheme (Fringer et al., 2006; Lai et al., 2010). If the flow is close to the

648 hydrostatic balance, the pressure of nonhydrostatic part will be so slight that the correction plays a minor

649 role. The key to the nonhydrostatic dynamics module is to solve the Poisson equation below.

$$\frac{\partial^2 p'_{nh}}{\partial x^2} + \frac{\partial^2 p'_{nh}}{\partial y^2} + \frac{\partial^2 p'_{nh}}{\partial z^2} = \frac{\rho_c}{\Delta t}\left(\frac{\partial \tilde{u}}{\partial x} + \frac{\partial \tilde{v}}{\partial y} + \frac{\partial \tilde{w}}{\partial z}\right) \tag{A.1}$$

650   The right-hand side (RHS) of this Eq. (A.1) is the divergence about the intermediate velocity as a

651 source or sink term. Here, based on the definition about divergence, the three components calculated

652 directly at each cell are specified in the three orthogonal coordinates as

$$\frac{\partial \tilde{u}}{\partial x} = \frac{\tilde{u}_{i,j}^k * Au_{i,j}^k - \tilde{u}_{i-1,j}^k * Au_{i-1,j}^k}{\Omega_{i,j}^k} \tag{A.2}$$

$$\frac{\partial \tilde{v}}{\partial y} = \frac{\tilde{v}_{i,j-1}^k * Av_{i,j-1}^k - \tilde{v}_{i,j}^k * Av_{i,j}^k}{\Omega_{i,j}^k} \tag{A.3}$$

$$\frac{\partial \tilde{w}}{\partial z} = \frac{\tilde{w}_{i,j}^k * Aw_{i,j} - \tilde{w}_{i,j}^{k+1} * Aw_{i,j}}{\Omega_{i,j}^k} \tag{A.4}$$

653   In Eqs. (A.2) to (A.4), i, j and k are the indices of increasing eastward, northward, and

654 downward along x, y, and z-axis, respectively, where $z = 0$ is defined on the undisturbed sea surface by

655 means of Cartesian coordinate system. $\tilde{u}$, $\tilde{v}$, and $\tilde{w}$ are the intermediate velocity; Au, Av and Aw

656 means the six faces area of a cell in i, j and k directions; Ω is the volume of a cell. Compared to the

657 finite difference method, the definition of the divergence of a cell is more accurate and reliable especially

658 when adjacent to the solid boundaries for the RHS calculation. The left-hand side (LHS) of this equation

659 is discretized horizontally on the Arakawa C-grid (Arakawa and Lamb, 1977) using the central difference

660 method with a second-order accuracy, and the vertical discretization is the same as Max-Planck-Institute

661 ocean model (Marsland et al., 2003), which is able to acquire the following finite discrete equation about

662 7 cells for nonhydrostatic pressure perturbation as

$$LHS = (XW)p'^k_{i-1,j} + (XE)p'^k_{i+1,j} + (YN)p'^k_{i,j+1} + (YS)p'^k_{i,j-1} + (ZU)p'^{k-1}_{i,j}$$
$$+ (ZD)p'^{k+1}_{i,j} + (XC + YC + ZC)p'^k_{i,j} \qquad (A.5)$$

663   In Eq. (A.5) the coefficients of the discretized LHS are given as follows.

$$XW = \frac{1}{DXu_{i-1,j} * DXp_{i,j}}, \qquad XE = \frac{1}{DXu_{i,j} * DXp_{i,j}},$$

$$YN = \frac{1}{DYv_{i,j-1} * DYp_{i,j}}, \qquad YS = \frac{1}{DYv_{i,j} * DYp_{i,j}},$$

$$ZU = \frac{1}{DZw^k_{i,j} * DZp^k_{i,j}}, \qquad ZD = \frac{1}{DZw^{k+1}_{i,j} * DZp^k_{i,j}},$$

$$XC = -\left(\frac{1}{DXu_{i-1,j}} + \frac{1}{DXu_{i,j}}\right)\frac{1}{DXp_{i,j}},$$

$$YC = -\left(\frac{1}{DYv_{i,j-1}} + \frac{1}{DYv_{i,j}}\right)\frac{1}{DYp_{i,j}},$$

$$ZC = -\left(\frac{1}{DZw^{k+1}_{i,j}} + \frac{1}{DZw^k_{i,j}}\right)\frac{1}{DZp^k_{i,j}} \qquad (A.6)$$

664   The DX, DY and DZ represent the spacing difference between the adjacent grid cells in x, y, and

665   z-axis. The suffixes associate u, v and w at cell face center and p' at body center. Thus, invoking the

666   boundary conditions (20) and Eqs. (A.5) to (A.6), the discretized Poisson equation with 7 cells can be

667   derived with the matrix form below

$$Ap'_{nh} = B \qquad (A.7)$$

668   Where A is a sparse, and definite-positive matrix with seven diagonals; p'_{nh} and B are the

669   column vectors with a size of all cell number $Nxyz = Nx \times Ny \times Nz$ in the model domain where Nx,

670   Ny, and Nz are the cell number in i, j and k directions. Actually, the sparse matrix A is too huge to

671   handle directly with a size of $Nxyz \times Nxyz$, which needs to be designed with greater efficiency as a

672   precondition. To apply the nonhydrostatic model to the real oceanic environment on the original model

673   base, the Portable, Extensible Toolkit for Scientific Computation (PETSc) Library is implemented into

674   the nonhydrostatic dynamic module. We apply the numerical Krylov subspace methods for the matrix

675   solvers under an MPI-based framework (Balay et al., 2020). Here, the Flexible Generalized Minimal

676   Residual (FGMRES) method (Saad, 1993) is employed to solve the equation (A.7) in conjunction with

677   a multigrid preconditioner (Smith et al. 1996) for the sparse matrix before iteration. With these methods

678   the nonhydrostatic dynamics can be fulfilled economically in harmony with the original numerical

679   framework.

Appendix B

The Korteweg–de Vries (KdV) Model in the Shallow Water

Based on the shallow water approximation, a small-amplitude internal solitary wave whose amplitude compared with the total depth is small enough can be described by the classical two-dimensional Korteweg-de Vries (KdV) equation given as follows (Apel et al., 2007)

$$\frac{\partial \eta}{\partial t} + c\frac{\partial \eta}{\partial x} + \alpha\eta\frac{\partial \eta}{\partial x} + \beta\frac{\partial^3 \eta}{\partial x^3} = 0 \tag{B.1}$$

Considering two-fluid stratification system is more appropriate for the experiments in Sec. 3.1–3.3. ρ_1 and ρ_2 are the upper and lower densities corresponding to the thickness h_1 and h_2; x is the horizontal coordinate. Several parameters can be written here as (Benjamin, 1966; Wessels and Hutter, 1996)

$$\alpha = -\frac{3c}{2}\frac{\rho_1 h_2^2 - \rho_2 h_1^2}{\rho_1 h_1 h_2^2 + \rho_2 h_1^2 h_2}, \beta = \frac{c}{6}\frac{\rho_1 h_1^2 h_2 + \rho_2 h_1 h_2^2}{\rho_1 h_2 + \rho_2 h_1}, c = \sqrt{\frac{g h_1 h_2 (\rho_2 - \rho_1)}{\rho_1 h_2 + \rho_2 h_1}} \tag{B.2}$$

where nonlinear and dispersion parameters (α and β respectively) can represent the soliton polarity; c is the linear velocity and the solution of solitary wave is expressed below the interface displacement $\eta(x, t)$

$$\eta(x, t) = \eta_0 sech^2\left(\frac{x - Vt}{L}\right) \tag{B.3}$$

in which the η_0 is the amplitude. The nonlinear velocity V (also called phase velocity) and the characteristic length of soliton L are given as

$$V = c + \frac{\alpha}{3}\eta_0, \qquad L = \sqrt{\frac{12\beta}{\alpha\eta_0}} \tag{B.4}$$

The dispersion parameter β is almost larger than zero for the internal solitary waves in the ocean but the sign for the nonlinear parameter α is relevant to the wave formation. When $\alpha > 0$, the interface displacement will show a waveform of depression soliton. If negative, the isopycnal elevation will appear. Therefore, the reverse situation for an internal solitary wave is determined by the sign change of the nonlinear parameter. The KdV model is suitable with weakly nonlinear and dispersive waves which is capable of being used to validate the small-amplitude ISW results in the laboratory. Nevertheless, when nonlinearity enhancement happens by the reason of shallower topography or stronger stratification, the modified KdV (m-KdV) model (Michallet and Barthelemy, 1998; GrimShaw et al., 2004) can describe

703   relatively stronger nonlinear solitons with the addition for cubic nonlinearity term as

$$\frac{\partial \eta}{\partial t} + (c + \alpha \eta - \alpha_1 \eta^2)\frac{\partial \eta}{\partial x} + \beta \frac{\partial^3 \eta}{\partial x^3} = 0 \tag{B.5}$$

704   It is worthy of noting that the m-KdV equation takes the higher-order nonlinear term into account

705   and can degenerate into the KdV equation when the cubic nonlinear parameter $\alpha_1 = 0$. Here, the solution

706   is given with the interface displacement $\eta(x,t)$

$$\eta(x,t) = \frac{\eta_0 sech^2\left(\frac{x-Vt}{L}\right)}{1 - \mu \, tanh^2\left(\frac{x-Vt}{L}\right)} \tag{B.6}$$

707   where

$$h_c = \frac{h_1 + h_2}{1 + \sqrt{\rho_1/\rho_2}}, \qquad \bar{h} = h_2 - h_c,$$

$$\mu = \begin{cases} h''/h' , & \bar{h} > 0 \\ h'/h'' , & \bar{h} < 0 \end{cases},$$

$$h' = -\bar{h} - |\bar{h} + \eta_0|, \qquad h'' = -\bar{h} + |\bar{h} + \eta_0|,$$

$$V = c_{0m}\left[1 - \frac{1}{2}\left(\frac{\bar{h} + \eta_0}{h_1 + h_2 - h_c}\right)^2\right],$$

$$c_{0m} = \left\{\frac{g(h_1 + h_2)}{2}\left[1 - \left(1 - \frac{4h_c(h_1 + h_2 - h_c)(\rho_2 - \rho_1)}{\rho_2(h_1 + h_2)^2}\right)^{1/2}\right]\right\}^{1/2},$$

$$L = 2(h_1 + h_2 - h_c)\sqrt{\frac{(h_1 + h_2 - h_c)^3 + h_c^3}{3(h_1 + h_2)h'h''}} \tag{B.7}$$

708   More generally, when considering the continuously stratified fluid, the linear velocity c refers to

709   the long-wave velocity of each mode for the Strum-Liouville problem given as follows (Apel et al., 2007)

$$\begin{cases} \frac{d^2 W}{dz^2} + \frac{N^2}{c^2}W = 0 \\ W = 0, & z = 0 \\ W = 0, & z = -H \end{cases} \tag{B.8}$$

710   where H is the water depth; N is the buoyancy frequency; W is the nondimensional modal function.

711   When the nonlinear and dispersion parameters (α and β respectively) are obtained as

$$\alpha = \frac{3c\int_{-H}^{0}(dW/dz)^3 \, dz}{2\int_{-H}^{0}(dW/dz)^2 dz}, \qquad \beta = \frac{c\int_{-H}^{0}W^2 \, dz}{2\int_{-H}^{0}(dW/dz)^2 dz} \tag{B.9}$$

712   Besides, if still considering the background current $\bar{U}(z)$, the Taylor-Goldstein equation (Miles,

713   1961; Liu, 2010) can describe the vertical modal function W, when the nonlinear and dispersion

714   parameters are obtained under the Boussinesq approximation expressed as (GrimShaw et al., 2002).

$$\frac{d^2\hat{\varphi}(z)}{dz^2} + \left[\frac{N^2}{(\overline{U}-c)^2} - \frac{\overline{U}''}{(\overline{U}-c)} - k^2\right]\hat{\varphi}(z) = 0 \tag{B.10}$$

$$\alpha = \frac{3\int_{-H}^{0}(c-\overline{U})^2\left(\frac{dW}{dz}\right)^3 dz}{2\int_{-H}^{0}(c-\overline{U})\left(\frac{dW}{dz}\right)^2 dz}, \quad \beta = \frac{\int_{-H}^{0}(c-\overline{U})^2 W^2 dz}{2\int_{-H}^{0}(c-\overline{U})\left(\frac{dW}{dz}\right)^2 dz} \tag{B.11}$$

715   where c is the n-mode linear speed; $\hat{\varphi}(z)$ is the stream function; $\overline{U}''$ are the second derivative of

716   background currents; k is the horizontal wave number.

717

Geoscientific
Model Development
Discussions

Code and data availability.

The current version of the nonhydrostatic ocean model (ORCTM-v1) and these experiments about the internal solitary wave simulation in this paper are available through https://doi.org/10.5281/zenodo.6683597 (HaoHuang, 2022), as well as the experiment configurations, preprocessing, and post-processing. The PETSc library (the download address: https://petsc.org/release/download/, Balay et al., 2020) needs to be installed before building the model. Nevertheless, we also provide the PETSc library of the version in use and the ORCTM quick manual for the users at the above link.

Author contributions.

HH and PS developed the nonhydrostatic dynamic framework in ORCTM and devised the internal solitary wave validation experiments. SQ and JG developed the open boundary module. HH and SQ analyzed the model results and interpreted the concepts, and all authors contributed to the writing of the paper.

Competing interest.

The authors of this paper declare that they have no conflicts of interest.

Reference

Arakawa, A., and Lamb, V. R.: Computational design of the basic dynamical processes of the UCLA general circulation model, Methods. Comput. Phys. 17, 173–265. https://doi.org/10.1016/B978-0-12-460817-7.50009-4, 1977.

Apel, J. R., Ostrovsky, L. A., Stepanyants, Y. A., and Lynch, J. F.: Internal solitons in the ocean and their effect on underwater sound, J. Acoust. Soc. Am., 121, 695-722, https://doi.org/10.1121/1.2395914, 2007.

750   Armfield, S. and Street, R.: An analysis and comparison of the time accuracy of fractional-step methods
751   for the Navier–Stokes equations on staggered grids, Int. J. Numer. Meth. Fl., 38, 255-282,
752   https://doi.org/10.1002/fld.217, 2002.
753   Arbic, B. K., and Scott, R. B.: On quadratic bottom drag, geostrophic turbulence, and oceanic mesoscale
754   eddies, J. Phys. Oceanogr. 38, 84-103, https://doi.org/10.1175/2007JPO3653.1, 2008.
755   Benjamin, T. B.: Internal waves of finite amplitude and permanent form, J. Fluid. Mech., 25, 241-270,
756   https://doi.org/10.1017/S0022112066001630, 1966.
757   Baines, P. G.: On internal tide generation models, Deep-Sea. Res., 29, 307-338,
758   https://doi.org/10.1016/0198-0149(82)90098-X, 1982.
759   Bourgault, D. and Kelley, D. E.: A laterally averaged nonhydrostatic ocean model, J. Atmos. Ocean. Tech.,
760   21, 1910-1924, https://doi.org/10.1175/JTECH-1674.1, 2004.
761   Buijsman, M. C., Kanarska, Y., and McWilliams, J. C.: On the generation and evolution of nonlinear
762   internal waves in the South China Sea, J. Geophys. Res.-Ocean, 115, C02012,
763   https://doi.org/10.1029/2009JC005275, 2010a.
764   Buijsman, M. C., McWilliams, J. C., and Jackson, C. R.: East-west asymmetry in nonlinear internal
765   waves from Luzon Strait, J. Geophys. Res.-Ocean, 115, C10057, https://doi.org/
766   10.1029/2009JC006004, 2010b.
767   Balay, S., Abhyankar, S., Adams, Mark F., Brown, J., Brune, P., Buschelman, K., Dalcin, L., Dener, A.,
768   Eijkhout, V., Gropp, W., Karpeyev, D., Kaushik, D., Knepley, M., May, D., McInnes, L. Curfman,
769   Mills, R., Munson, T., Rupp, K., Sanan, P., Smith, B., Zampini, S., Zhang, H., and Zhang, H.: PETSc
770   Users Manual, Tech. Rep. ANL-95/11-Revision 3.13, Argonne National Laboratory,
771   https://doi.org/10.2172/1614847, 2020.
772   Chorin, A. J.: Numerical solution of the Navier–Stokes equations, Math. Comput., 22, 745-762,
773   https://doi.org/10.2307/2004575, 1968.
774   Chen, C., Liu, H., and Beardsley, R. C.: An unstructured grid, finite-volume, three-dimensional, primitive
775   equations ocean model: application to coastal ocean and estuaries, J. Atmos. Ocean. Tech., 20, 159-
776   186, https://doi.org/10.1175/1520-0426(2003)020<0159:AUGFVT>2.0.CO;2, 2003.
777   Chen, X., Jungclaus, J., Thomas, M., Maier-Reimer, E., Haak, H., and Suendermann, J.: An oceanic
778   general circulation and tide model in orthogonal curvilinear coordinates, Amer. Geophys. Union.,
779   Fall Meeting 2005, San Francisco, CA, December 2005, Abstract OS41B-0600, 2005.
780   Chen, Z., Nie, Y., Xie, J., Xu, J., He, Y., and Cai, S.: Generation of internal solitary waves over a large
781   sill: From Knight Inlet to Luzon Strait, J. Geophys. Res.-Ocean, 122, 1555–1573.
782   https://doi.org/10.1002/2016JC012206, 2017.
783   Cushman-Roisin, B.: Kelvin–Helmholtz instability as a boundary-value problem. Environ. Fluid.
784   Mech., 5, 507-525, https://doi.org/10.1007/s10652-005-2234-0, 2005.
785   Duda, T. F., Morozov, A. K., Howe, B. M., Brown, M. G., Speer, K., Lazarevich, P., Worcester, P. F., and
786   Cornuelle, B. D.: Evaluation of a long-range joint acoustic navigation/thermometry system, Oceans-
787   IEEE., 1-6, https://doi.org/10.1109/OCEANS.2006.306999, 2006.
788   Fofanoff, P., and Millard, R. C.: Algorithms for computation of fundamental properties of seawater,
789   Unesco. R. M., 44, 203-209, https://doi.org/10.1016/j.saa.2012.12.093, 1983.
790   Fringer, O. B., Gerritsen, M., and Street, R. L.: An unstructured-grid, finite-volume, nonhydrostatic,
791   parallel coastal ocean simulator, Ocean. Model., 14, 139-173,
792   https://doi.org/10.1016/j.ocemod.2006.03.006, 2006.
793   Gilbert, D., and Garrett, C.: Implications for ocean mixing of internal wave scattering off irregular

794   topography, J. Phys. Oceanogr., 19, 1716-1729, https://doi.org/10.1175/1520-
795   0485(1989)019<1716:IFOMOI>2.0.CO;2, 1989.

796   Gerkema, T., and Zimmerman, J. T. F.: Generation of nonlinear internal tides and solitary waves, J. Phys.
797   Oceanogr., 25, 1081-1094, https://doi.org/10.1175/1520-0485(1995)0252.0.CO;2, 1995.

798   Grue, J., Jensen, A., Rusås, P. O., and Sveen, J. K.: Breaking and broadening of internal solitary waves,
799   J. Fluid. Mech., 413, 181-217, https://doi.org/10.1017/S0022112000008648, 2000.

800   GrimShaw, R., PelinovSky, E., and Poloukhina, O.: Higher-order Korteweg-de Vries models for internal
801   solitary waves in a stratified shear flow with a free surface, Nonlinear. Proc. Geoph., 9, 221-235,
802   https://doi.org/10.5194/npg-9-221-2002, 2002.

803   Grimshaw, R., Pelinovsky, E., Talipova, T., and Kurkin, A.: Simulation of the transformation of internal
804   solitary waves on oceanic shelves, Journal of physical oceanography, J. Phys. Oceanogr., 34, 2774-
805   2791, https://doi.org/10.1175/JPO2652.1, 2004.

806   Garrett, C., and Kunze, E.: Internal tide generation in the deep ocean, Annu. Rev. Fluid. Mech., 39, 57-
807   87, https://doi.org/10.1146/annurev.fluid.39.050905.110227, 2007.

808   Helfrich, K. R., and Melville, W. K.: On long nonlinear internal waves over slope-shelf topography, J.
809   Fluid. Mech., 167, 285-308, http://dx.doi.org/10.1017/S0022112086002823, 1986.

810   Härtel, C., Meiburg, E., and Necker, F.: Analysis and direct numerical simulation of the flow at a gravity-
811   current head. Part 1. Flow topology and front speed for slip and no-slip boundaries, J. Fluid. Mech.,
812   418, 189-212, http://dx.doi.org/10.1017/s0022112000001221, 2000.

813   Huang, X., Chen, Z., Zhao, W., Zhang, Z., Zhou, C., Yang, Q., and Tian, J.: An extreme internal solitary
814   wave event observed in the northern South China Sea, Sci. Rep-UK., 6, 1-10,
815   http://dx.doi.org/10.1038/srep30041, 2016.

816   HaoHuang.: HuangOCEAN02/ORCTM: ORCTM v1.1.1 (ORCTMv1.1.1), Zenodo [code],
817   https://doi.org/10.5281/zenodo.6683597, 2022.

818   Kanarska, Y., Shchepetkin, A., McWilliams, J. C.: Algorithm for non-hydrostatic dynamics in the
819   regional oceanic modeling system, Ocean. Model., 18, 143-174,
820   http://dx.doi.org/10.1016/j.ocemod.2007.04.001, 2007.

821   Ko, D. S., Martin, P. J., Rowley, C. D., and Preller, R. H.: A real-time coastal ocean prediction experiment
822   for MREA04, J. Marine. Syst., 69, 17-28, http://dx.doi.org/10.1016/j.jmarsys.2007.02.022, 2008.

823   Lawrence, G. A., Browand, F. K., and Redekopp, L. G.: The stability of a sheared density interface, Phys.
824   Fluids. A-FLUID., 3, 2360-2370, https://doi.org/10.1063/1.858175, 1991.

825   Legg, S., and Adcroft, A.: Internal wave breaking at concave and convex continental slopes, J. Phys.
826   Oceanogr., 33, 2224-2246, https://doi.org/10.1175/1520-
827   0485(2003)033<2224:IWBACA>2.0.CO;2, 2003.

828   Legg, S., and Klymak, J.: Internal hydraulic jumps and overturning generated by tidal flow over a tall
829   steep ridge, J. Phys. Oceanogr., 38, 1949-1964, https://doi.org/10.1175/2008JPO3777.1, 2008.

830   Lai, Z., Chen, C., Cowles, G. W., and Beardsley, R. C.: A nonhydrostatic version of FVCOM: 1.
831   Validation experiments, J. Geophys. Res.-Ocean, 115, C11010,
832   https://doi.org/10.1029/2009JC005525, 2010.

833   Liu, Z.: Instability of baroclinic tidal flow in a stratified fjord, J. Phys. Oceanogr., 40, 139-154,
834   https://doi.org/10.1175/2009JPO4154.1, 2010.

835   Liu. Z., Lin, L., Xie, L., and Gao, H.: Partially implicit finite difference scheme for calculating dynamic
836   pressure in a terrain-following coordinate non-hydrostatic ocean model, Ocean. Model., 106, 44-57,
837   https://doi.org/10.1016/j.ocemod.2016.09.004, 2016.

838 Li, J., Zhang, Q., and Chen, T.: ISWFoam: A numerical model for internal solitary wave simulation in
839   continuously stratified fluids, Geosci. Model. Dev., 15, 105–127, https://doi.org/10.5194/gmd-15-
840   105-2022, 2022.
841 Miles, J. W.: On the stability of heterogeneous shear flows, J. Fluid. Mech., 10, 496-508,
842   https://doi.org/10.1017/S0022112061000305, 1961.
843 Mtfller, P.: On the diffusion of momentum and mass by internal gravity waves, J. Fluid. Mech., 77, 789-
844   823, https://doi.org/10.1017/S0022112076002899, 1976.
845 Marshall, J., Hill, C., Perelman, L., and Adcroft, A.: Hydrostatic, quasi-hydrostatic, and nonhydrostatic
846   ocean modeling, J. Geophys. Res.-Ocean, 102, 5733-5752, https://doi.org/10.1029/96JC02776,
847   1997a.
848 Marshall, J., Adcroft, A., Hill, C., Perelman L., and Heisey, C.: A finite-volume, incompressible Navier
849   Stokes model for studies of the ocean on parallel computers, J. Geophys. Res.-Ocean, 102, 5753-
850   5766, https://doi.org/10.1029/96JC02775, 1997b.
851 Marshall, J., Jones, H., and Hill, C.: Efficient ocean modeling using non-hydrostatic algorithms, J.
852   Marine. Syst., 18, 115-134, https://doi.org/10.1016/S0924-7963(98)00008-6, 1998.
853 Michallet, H., and Barthélemy, E.: Experimental study of interfacial solitary waves, J. Fluid. Mech., 366,
854   159-177, https://doi.org/10.1017/S002211209800127X, 1998.
855 Michallet, H., and Ivey, G. N.: Experiments on mixing due to internal solitary waves breaking on uniform
856   slopes, J. Geophys. Res.-Ocean, 104, 13467-13477, https://doi.org/10.1029/1999JC900037, 1999.
857 Marsland, S. J., Haak, H., Jungclaus, J. H., Latif, M. and Röske, F.: The Max-Planck-Institute global
858   ocean/sea ice model with orthogonal curvilinear coordinates, Ocean. Model., 5, 91-127,
859   https://doi.org/10.1016/S1463-5003(02)00015-X, 2003.
860 Ma, Q., Yuan, C., Lin, X., and Chen, X.: The investigation of internal solitary waves over a continental
861   shelf-slope, J. Oceanol. Limnol., 38, 695-706, https://doi.org/10.1007/s00343-019-9123-8, 2020.
862 Ono, H.: Algebraic solitary waves in stratified fluids, J. Phys. Soc. Jpn., 39, 1082-1091,
863   https://doi.org/10.1143/JPSJ.39.1082, 1975.
864 Osborne, A. R., Burch, T. L., and Scarlet, R. I.: The influence of internal waves on deep-water drilling,
865   J. Pet. Technol., 30, 1497-1504, https://doi.org/10.2118/6913-PA, 1978.
866 Pacanowski, R. C., and Philander, S. G. H.: Parameterization of vertical mixing in numerical models of
867   tropical oceans, J. Phys Oceanogr., 11, 1443-1451, https://doi.org/10.1175/1520-
868   0485(1981)011<1443:POVMIN>2.0.CO;2, 1981.
869 Press, W. H., Flannery, B. P., Teukolsky, S. A., and Vetterling, W. T., Numerical Recipes in C. The Art of
870   Scientific Computing, Cambridge University Press, 1988.
871 Ramp, S. R., Tang, T. Y., Duda, T. F., Lynch, J. F., Liu, A. K., Chiu, C. S., Bahr, F. L., Kim, H. R., and
872   Yang, Y. J.: Internal solitons in the northeastern South China Sea. Part I: Sources and deep water
873   propagation, IEEE. J. Oceanic. Eng., 29, 1157-1181, https://doi.org/1157-
874   1181,10.1109/JOE.2004.840839, 2004.
875 Ramp, S. R., Park, J. -H., Yang, Y. J., Bahr, F. L., and Jeon, C.: Latitudinal Structure of Solitons in the
876   South China Sea, J. Phys. Oceanogr., 49, 1747-1767, https://doi.org/10.1175/JPO-D-18-0071.1,
877   2019.
878 Saad Y.: A flexible inner-outer preconditioned GMRES algorithm, SIAM J. Sci. Comput., 14, 461-469,
879   https://doi.org/10.1137/0914028, 1993.
880 Smith, B., Bjorstad, P., and Gropp, W.: Domain Decomposition: Parallel Multilevel Methods for Elliptic
881   Partial Differential Equations. Cambridge University Press, 1996.

Stansby, P. K., and Zhou, J. G.: Shallow-water flow solver with non-hydrostatic pressure: 2D vertical plane problems, Int. J. Numer. Meth. Fluids, 28, 541-563, https://doi.org/10.1002/(SICI)1097-0363(19980915)28:33.0.CO;2-0, 1998.

Shchepetkin, A. F., and McWilliams, J. C.: The regional oceanic modeling system (ROMS): a split-explicit, free-surface, topography-following-coordinate oceanic model, Ocean. Model., 9, 347-404, https://doi.org/10.1016/j.ocemod.2004.08.002, 2005.

Shaw, P. T., Ko, D. S., and Chao, S. Y.: Internal solitary waves induced by flow over a ridge: With applications to the northern South China Sea, J. Geophys. Res.-Ocean, 114, C02019, https://doi.org/10.1029/2008JC005007, 2009.

Vlasenko, V., Hutter, K.: Numerical experiments on the breaking of solitary internal waves over a slope–shelf topography, J. Phys. Oceannogr., 32, 1779-1793, https://doi.org/10.1175/1520-0485(2002)032<1779:NEOTBO>2.0.CO;2, 2002.

Vlasenko, V., Stashchuk, N., and Hutter, K.: Baroclinic tides: theoretical modeling and observational evidence, Cambridge University Press, 2005.

Vlasenko, V., Stashchuk, N., Guo, C., and Chen, X.: Multimodal structure of baroclinic tides in the South China Sea, Nonlinear. Proc. Geoph., 17, 529-543, https://doi.org/10.5194/npg-17-529-2010, 2010.

Wessels, F., and Hutter, K.: Interaction of internal waves with a topographic sill in a two-layered fluid, J. Phys. Oceanogr., 26, 5-20, https://doi.org/10.1175/1520-0485(1996)026<0005:IOIWWA>2.0.CO;2, 1996.

Wolff, J. O., Maier-Reimer, E., and Legutke, S.: The Hamburg ocean primitive equation model, Tech. Rep. No. 13, German Climate Computer Center (DKRZ), Hamburg, Germany, 1997.

Wang,Y. H., Dai, C. F., and Chen, Y. Y.: Physical and ecological processes of internal waves on an isolated reef ecosystem in the South China Sea, Geophys. Res. Lett., 34, 312-321, https://doi.org/10.1029/2007GL030658, 2007.

Zhao, Z., and Alford, M. H.: Source and propagation of internal solitary waves in the northeastern South China Sea, J. Geophys. Res.-Ocean, 111, C11012, https://doi.org/10.1029/2006JC003644, 2006.

Zheng, Q., Susanto, R. D., Ho, C. R., Song, Y. T., and Xu, Q.: Statistical and dynamical analyses of generation mechanisms of solitary internal waves in the northern South China Sea, J. Geophys. Res.-Ocean, 112, C0302, https://doi.org/10.1029/2006JC003551, 2007.

Zhang, Z., Fringer, O. B., and Ramp, S. R.: Three-dimensional, nonhydrostatic numerical simulation of nonlinear internal wave generation and propagation in the South China Sea, J. Geophys. Res.-Ocean, 116, C05022, https://doi.org/10.1029/2010JC006424, 2011.

Zeng, Z., Chen, X., Yuan, C., Tang, S., and Chi, L.: A numerical study of generation and propagation of type-a and type-b internal solitary waves in the northern South China Sea, Acta Oceanol. Sin., 38, 20-30, https://doi.org/10.1007/s13131-019-1495-2, 2019.